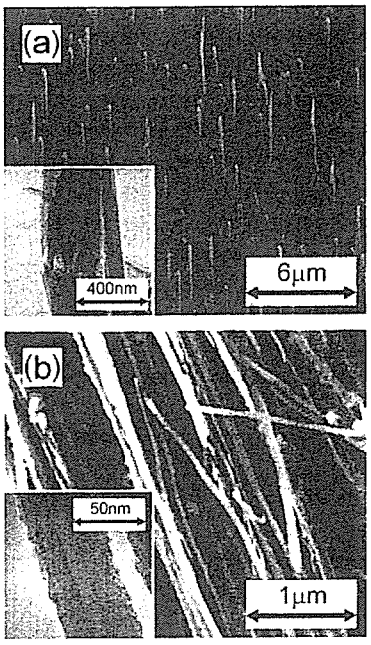

Fig. 3. SEM and TEM images showing the MWNTs on the rf electrode under the conditions of (a) B_z=0.03 T and V_{RFE}=−200 V (floating) and (b) B_z=2 T and V_{RFE}=−200 V.

corresponds to the energy of ions across the magnetic field is described as

$$v_{di} = \left(\mu E - D\frac{\nabla n}{n}\right)\frac{1}{1+(\omega_c\tau)^2},$$

where E, $\nabla n/n$, μ, and D are the sheath electric field, a density gradient in front of the rf electrode, mobility, and diffusion coefficient of the ions, respectively. The effect of the magnetic field is included as $\omega_c\tau$, where $\omega_c/2\pi$ is an ion cyclotron frequency and τ is a collision time between ion and neutral gas. The magnetic field is found to effectively decrease the ion drift velocity, i.e., ion energy. The calculated ion energy is about 130 eV and almost consistent with the sheath voltage ($|V_{sh}|$=130 V) at B_z=0.03 T, while the ion energy is found to become extremely low (~2 eV) at B_z=2 T in spite of the existence of the large sheath electric field. This is because the acceleration of ions along the sheath electric field is prevented by trapping around the magnetic-field lines, i.e., magnetization of ions.

In order to investigate the effects of the strong magnetic field on the nanotube formation, the plasma system for the nanotube growth is operated at (a) B_z=0.03 T and V_{RFE}=−200 V (floating) and (b) B_z=2 T and V_{RFE}=−200 v, which are based on the experimental results of measuring the plasma parameter as shown by arrows with alphabetic letters in Fig. 2. It is to be noted that the floating potential of the rf electrode (V_{RFE}=−200 V) at B_z=0.03 T is different from the results in Fig. 2 (V_{RFE}=−110 V), because methane and hydrogen are used for the nanotube formation instead of argon and the rf power is increased to 1400 W. The carbon nanotubes grow across the magnetic field lines in both the cases of B_z=0.03 and 2 T. This means that the carbon nanotubes are aligned along the sheath electric field in front of the rf electrode as the substrate even in the strong magnetic field.

Fig. 3 presents scanning electron microscopy (SEM) images of the row soot deposited on the Ni rf electrode surface after the 60 min discharge in each case of the plasma parameter described above. It is found that well-aligned multi-walled carbon nanotubes (MWNTs) are successfully formed in both the weak and strong magnetic fields. However, it is noted that the nanotube structure at B_z=0.03 T is very thick as shown in Fig. 3(a). According to the analysis by transmission electron microscopy (TEM), which is shown in the inset, it is found that a few MWNTs combine with each other and form the thick nanotube-like graphitic material. In this case, since the ions are accelerated by the negative V_{sh} in front of the rf electrode as shown in Fig. 2 and impinge on the rf electrode with high energy, the generated MWNTs are considered to be deformed by the bombardment of the high energy ions. When the strong magnetic field is applied perpendicularly to the sheath electric field, the magnetic field prevents the high energy ions from directly impinging on the rf electrode due to the magnetization of ions, even if the large sheath electric field exists. Thus, the MWNTs formed at B_z=2 T [Fig. 3(b)] are found to be well-aligned by the sheath electric field and not to be deformed due to the reduction of the ion bombardment energy toward the rf electrode. Here, it is confirmed that most of the products in the case of B_z=2 T and V_{RFE}=float-

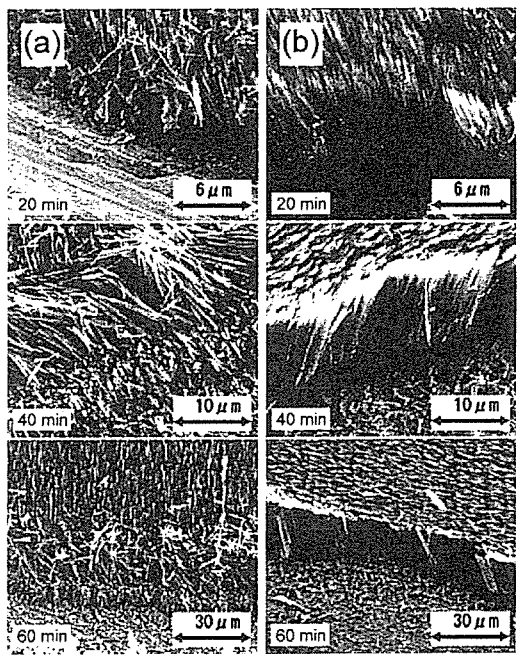

Fig. 4. Time evolutions of the nanotube growth in the SEM images under the conditions of (a) B_z=0.03 T and (b) B_z=2 T. The rf electrode is biased at V_{RFE}=−200 V.

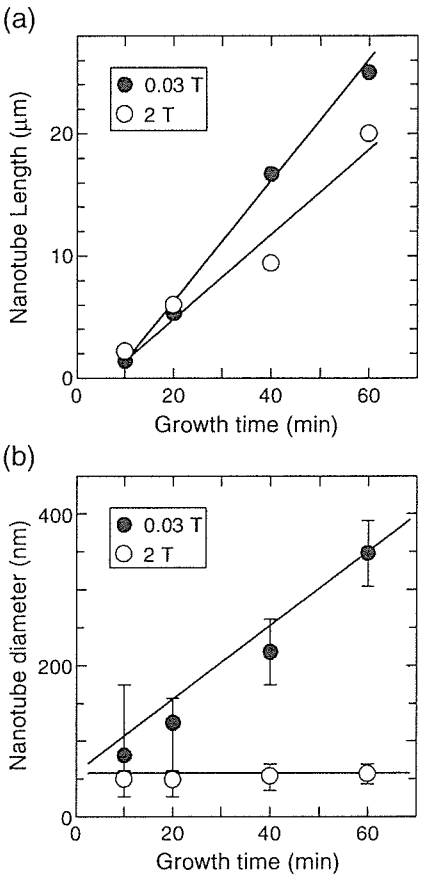

Fig. 5. Variations of nanotube (a) length and (b) diameter with growth time. The rf electrode is biased at $V_{RFE}=-200$ V.

ing (+60 V) consist of amorphous carbon, because the positive ions as a carbon source for the nanotube formation cannot reach to the rf electrode due to the positive V_{sh}, and as a result, the nanotubes cannot be formed.

The time evolution of the nanotube growth is shown in the SEM images in Fig. 4 at (a) $B_z=0.03$ T and (b) $B_z=2$ T. From Fig. 4(a), it is found that the MWNTs grow and also become thick as time goes by in the weak magnetic field (=0.03 T). In the case when the strong magnetic field (=2 T) is applied, on the other hand, the MWNTs grow in the same way as the case of $B_z=0.03$ T, but the thickness of the MWNTs remains thin even after 60 min growth.

The variation of nanotube length and diameter with growth time are summarized in Fig. 5(a) and (b), respectively. The nanotube growth rates for $B_z=0.03$ and 2 T are 0.4 and 0.33 μm/min, respectively. There is no significant difference in the growth rate when the applied magnetic field is changed. However, the nanotube diameter is drastically changed with the applied magnetic field. In the case of $B_z=0.03$ T, the nanotube diameter gradually increases with an increase in the growth time, while the diameter is temporally almost constant in the case of $B_z=2$ T, remaining the small diameter (~50 nm) which is determined at the beginning of the nanotube formation.

Based on our experimental results of the time evolution, MWNTs are formed in the same way in both the weak and strong magnetic fields up to about 10 min growth. After 10 min growth, however, MWNTs for $B_z=0.03$ T are found to be gradually deformed by the bombardment of the high energy ions and combine with each other, resulting in the thick nanotube like graphite materials.

4. Conclusion

Our experiments demonstrate that the multi-walled carbon nanotubes (MWNTs) are formed by plasma-enhanced chemical vapor deposition directly on the rf electrode under the condition of the strong magnetic field. When the magnetic field is weak ($B_z=0.03$ T), the self-bias voltage of the rf electrode attains to −200 V and the MWNTs on the rf electrode are deformed and combined with each other by the bombardment of the high energy ions. When the strong magnetic field ($B_z=2$ T) is applied, on the other hand, the MWNTs are observed not to be deformed and to grow well-aligned along the sheath electric field. This result can be explained by the reduction of the ion bombardment energy, which is caused by the magnetization of the ions for $B_z=2$ T. Finally, it is found that the controls of the sheath voltage and the ion bombardment energy by the magnetic field introduction have crucial effects on the nanotube growth.

Acknowledgements

We express our gratitude to H. Ishida and K. Motomiya for their technical support and useful discussion. This work was supported partly by the Foundation "Hattori-Hokokai", and partly by a Grant-in-Aid for Scientific Research from the Ministry of Education, Culture, Sports, Science and Technology, Japan.

References

[1] S. Fan, M.G. Chapline, N.R. Franklin, T.W. Tombler, A.M. Cassell, H. Dai, Science 283 (1999) 512.
[2] Y. Hayashi, T. Negishi, S. Nishino, J. Vac. Sci. Technol., A, Vac. Surf. Films 19 (2001) 1796.
[3] M. Meyyappan, L. Delzeit, A. Cassell, D. Hash, Plasma Sources Sci. Technol. 12 (2003) 205.
[4] H. Ishida, N. Satake, G.-H. Jeong, Y. Abe, T. Hirata, R. Hatakeyama, K. Tohji, K. Motomiya, Thin Solid Films 407 (2002) 26.
[5] N. Satake, G.-H. Jeong, T. Hirata, R. Hatakeyama, H. Ishida, K. Tohji, K. Motomiya, Physica B 323 (2002) 290.
[6] G.-H. Jeong, N. Satake, T. Kato, T. Hirata, R. Hatakeyama, K. Tohji, Jpn. J. Appl. Phys. 42 (2003) L1340.
[7] T. Hirata, N. Satake, G.-H. Jeong, T. Kato, R. Hatakeyama, K. Motomiya, K. Tohji, Appl. Phys. Lett. 83 (2003) 1119.
[8] H. Yokomichi, H. Sakima, M. Ichihara, F. Sakai, K. Itoh, N. Kishimoto, Appl. Phys. Lett. 74 (1999) 1827.

Available online at www.sciencedirect.com
SCIENCE DIRECT®
Journal of Physics and Chemistry of Solids 67 (2006) 1510–1517
JOURNAL OF PHYSICS AND CHEMISTRY OF SOLIDS
www.elsevier.com/locate/jpcs

Synthesis and magnetic properties of the size-controlled Mn–Zn ferrite nanoparticles by oxidation method

R. Justin Joseyphus[a], A. Narayanasamy[a,*], K. Shinoda[b], B. Jeyadevan[b], K. Tohji[b]

[a] *Materials Science Centre, Department of Nuclear Physics, University of Madras, Guindy Campus, Chennai 600 025, India*
[b] *Graduate School of Environmental Studies, Tohoku University, Aoba 4, Aramaki, Aoba-ku, Sendai 980-8579, Japan*

Received 24 May 2005; accepted 29 November 2005

Abstract

Size-controlled $Mn_{0.67}Zn_{0.33}Fe_2O_4$ nanoparticles in the wide range from 80 to 20 nm have been synthesized, for the first time, using the oxidation method. It has been demonstrated that the particle size can be tailor-made by varying the concentration of the oxidant. The magnetization of the 80 nm particles was 49 A m^2 kg^{-1} compared to 34 A m^2 kg^{-1} for the 20 nm particles. The Curie temperatures for all the samples are found to be within 630 ± 5 K suggesting that there is no size-dependent cation distribution. The critical particle size for the superparamagnetic limit is found to be about 25 nm. The effective magnetic anisotropy constant is experimentally determined to be 7.78 kJ m^{-3} for the 25 nm particles, which is about an order of magnitude higher than that of the bulk ferrite.
© 2006 Elsevier Ltd. All rights reserved.

Keywords: A. Nanostructures; A. Magnetic materials; B. Chemical synthesis; C. Mössbauer spectroscopy; D. Magnetic properties

1. Introduction

Ferrite nanoparticles find important applications in heat transfer devices, drug delivery systems and in medical diagnostics [1]. Nanosize particles of ferrites can be prepared using various synthesis techniques namely ball-milling [2], citrate precursor [3], hydrothermal [4], coprecipitation [5,6], and other chemical methods [7]. The magnetic properties of the ferrite nanoparticles are found to undergo changes due to superparamagnetism, surface spin effects and also with their cation distribution which depends on the method of synthesis [8–10]. Ferrites of the type AB_2O_4 where A and B are divalent and trivalent cations respectively possess the spinel structure. The oxygen ions form the f.c.c. structure and the cations occupy the interstitial positions. There are two interstitial sites, one being the tetrahedral or A-site surrounded by four oxygen ions and the other, octahedral or B-site surrounded by six oxygen ions. The exchange interaction in spinel ferrites where the antiparallel alignment of magnetic moments of A-site with B-site is mediated by oxygen ions is called superexchange interaction. The strength of the antiparallel coupling between the metal ions depends on the A–O–B bond angle with the strength being maximum for an angle of 180°. The interesting magnetic properties such as magnetization and Curie temperature of various ferrites have been observed to depend on the superexchange interaction strength, which is determined by the site occupancy of metal ions in the A- and B-sites. According to the site occupancy of the metal ions, the spinel ferrites are classified as normal spinel where the tetrahedral sites are occupied only by divalent metal ions, inverse spinel where all the divalent ions are present in the octahedral site and mixed spinel where divalent ions are present both in tetrahedral and octahedral sites. The magnetization and Curie temperature are found to vary with the distribution of cations in the A- and B-sites. The net magnetization is the result of the difference in the sublattice moments of the two sites, which depends upon the cation occupancy. Mössbauer spectroscopy has been effectively used in the study of cation distribution in spinel ferrites [11–14]. The Mössbauer parameters are also influenced by the type of ferrites and the superparamagnetic

*Corresponding author.
E-mail address: ansuom@yahoo.co.in (A. Narayanasamy).

0022-3697/$ - see front matter © 2006 Elsevier Ltd. All rights reserved.
doi:10.1016/j.jpcs.2005.11.015

behaviour due to smaller particle size [14,15]. Mössbauer spectroscopy has also been used to study the particle size-dependent magnetic ordering in ferrites like Ni–$ZnFe_2O_4$ [5] and Mn–$ZnFe_2O_4$ [16].

Small ferrite particles are found to exhibit superparamagnetic behaviour with their coercivity approaching zero. The critical particle size for superparamagnetism has also been calculated for various ferrites with the sizes being 14, 25 and 50 nm for the $CoFe_2O_4$, Fe_3O_4 and $MnFe_2O_4$, respectively [17]. The blocking temperature for the superparamagnetism of the nanoparticles depends on their magnetocrystalline anisotropy. A comparative study of $CoFe_2O_4$ and $MgFe_2O_4$ with 20 nm particle size has suggested that the blocking temperature of $CoFe_2O_4$ is higher than that of $MgFe_2O_4$ by 150 K which is due to the higher magnetocrystalline anisotropy of the former [18]. The blocking temperature not only depends on the magnetocrystalline anisotropy, but also on the particle size. The surface anisotropy adds to the total anisotropy in the case of small particles [19]. The blocking temperature increases with particle size due to increase in the anisotropy energy, KV compared to the thermal energy, k_BT. The anisotropy constant of $CoFe_2O_4$ particles of size about 3.3 nm is found to be $3.15 \times 10^6\,J\,m^{-3}$ which is an order of magnitude higher than that of the bulk materials [20].

The size-dependent magnetic properties of various ferrites have been studied for particles with particle sizes less than 25 nm synthesized using aqueous methods. The synthesis of larger particles involve heat treatment which leads to particle agglomeration. But a modified oxidation method yields non-agglomerated particles of size as large as 100 nm in $CoFe_2O_4$ where the nucleation rate is controlled by varying the concentration of ferric ions [21]. The $CoFe_2O_4$ with particle size of 20 nm synthesized through such methods is found to be non-superparamagnetic [22] due to their high magnetocrystalline anisotropy compared to Mn–Zn ferrites. Mn–Zn ferrites prepared through the hydrothermal route have resulted in smaller particle sizes [4]. The control over particle size to achieve better magnetic properties was attempted for Mn–Zn ferrites and a growth assisted coprecipitation had yielded magnetization as large as $50\,A\,m^2\,kg^{-1}$ compared to the value of $37\,A\,m^2\,kg^{-1}$ for the coprecipitated samples [23] with an average crystallite size of 12 nm. Tamura and Matijevic [24] have synthesized ferrite particles by using oxidation method with an emphasis on the shape rather than on the size of the particles. The maximum size that could be achieved, so far, for the Mn–Zn ferrite nanoparticles synthesized using oxidation method is 20 nm only [25].

Larger ferrite nanoparticles obtained from heat treatment are found to suppress the superparamagnetism. However, heat treatment would also enable the agglomeration of particles, which is not desirable. Hence it will be interesting to synthesize Mn–Zn nanoparticles with a higher upper limit for size in the as-prepared state itself and study the size-dependent variation in their magnetic properties. In this article we report the synthesis of $Mn_{0.67}Zn_{0.33}Fe_2O_4$ nanoparticles with the particle size ranging from 20 to 80 nm. The nanoparticles were characterized using X-ray diffraction and electron microscopic techniques. The magnetic properties and relaxation effects were also studied using a vibrating sample magnetometer (VSM) and Mössbauer spectroscopy, respectively. The magnetic nanoparticles were characterized with an emphasis on the determination of the critical size of the superparamagnetic particle and the effective magnetic anisotropy constant.

2. Experimental

$Mn_{0.67}Zn_{0.33}Fe_2O_4$ was synthesized by using analytical grade reagents of $FeSO_4 \cdot 7H_2O$, $MnCl_2 \cdot 4H_2O$, $ZnSO_4 \cdot H_2O$, and $Fe_2(SO_4)_3$ salts, wherever necessary, fixing the ratio of Mn to Zn as 2. NaOH was used for the metal hydroxide precipitation and KNO_3 was used to oxidize the ferrous ions to the ferric state. The Fe, Mn, and Zn salts were dissolved separately in water (250 mL) and the mixture of these solutions was allowed to react with NaOH dissolved in an equal amount of water. The metal hydroxide precipitate with a pH between 12 and 13 was oxidized with various amounts of KNO_3 in a round bottom flask at 363 K under constant mechanical stirring for 2 h. The resulting ferrite precipitate was washed several times with water and dried in an oven at 333 K for 48 h. The crystallographic phase analysis was carried out using a RIGAKU X-ray diffractometer with Cu-Kα radiation. The measurements were performed at 293 K in the 2θ range from 20° to 70°. The average grain size was calculated from the width of the (3 1 1) peak using the Scherrer formula. The average particle size was examined using a Hitachi scanning electron microscope (SEM) and also a Hitachi transmission electron microscope (TEM). The magnetic properties were studied using a Tamakawa VSM in a maximum applied field of 1 T. The Mössbauer spectra were recorded using a Wissel constant acceleration Mössbauer spectrometer with a $^{57}Co/Rh$ source kept at 293 K. The low-temperature Mössbauer experiments were performed from 293 to 16 K using a CTI-make closed cycle helium cryostat.

3. Results and discussion

3.1. The size-controlled synthesis of Mn–Zn ferrite

The ferrous hydroxide precipitate was oxidized with a mild oxidant such as KNO_3. The amount of KNO_3 determines the rate at which ferric ions are generated and determines the final particle size of the ferrites. Another method used to prepare larger particles is to introduce ferric ions along with ferrous ions at the beginning of the reaction itself thereby separating the nucleation and growth of the particles. The concentration of the ferric ions will decide the number of ferrite nuclei formed which

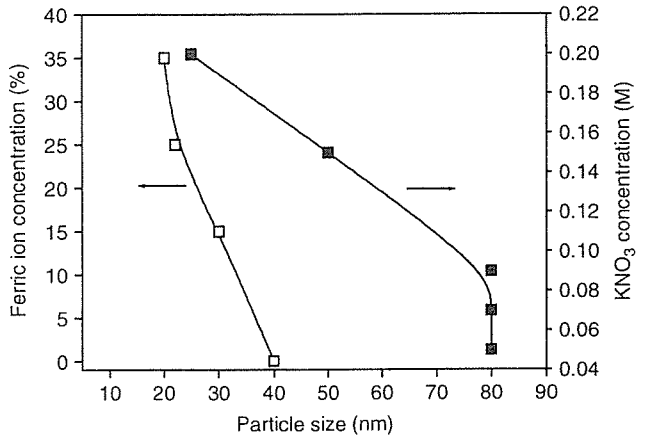

Fig. 1. The particle size variation with the concentration of ferric ions and KNO_3 (Connecting lines are guide to eye).

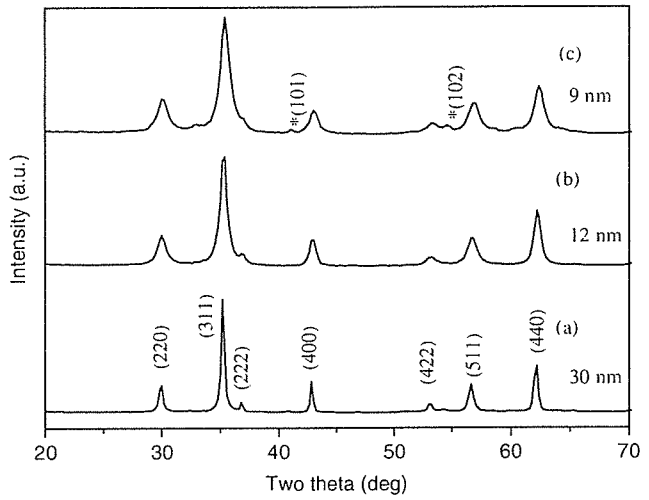

Fig. 2. The XRD pattern of $Mn_{0.67}Zn_{0.33}Fe_2O_4$ (a) sample A, (b) sample B, and (c) sample C with the average grain sizes of 30, 12, and 9 nm, respectively. (* represents MOOH impurity peak).

subsequently grow. Fig. 1 shows the particle size variation with the concentration of ferric ions and KNO_3. We shall restrict our discussions only to the ferrite nanoparticles with average particle size of 80, 25, and 20 nm synthesized using 0.09, 0.20 M of KNO_3, and 35% ferric ions and designated as sample A, B, and C, respectively for easy reference.

Fig. 2 shows the XRD pattern of (a) sample A, (b) sample B, and (c) sample C. The average grain size decreases from 30 nm for sample A to 12 and 9 nm for sample B and C, respectively. The formation of α-Fe_2O_3 during precipitation due to the loss of Zn^{2+} or Mn^{2+} ions has been reported for the hydrothermally synthesized [26] samples whereas only a small amount of MOOH impurity phase is present in sample C in the present study. Fig. 3(a) shows the SEM picture of sample A and Figs. 3(b) and (c) show the TEM photographs of samples B and C, respectively. For the sample A, the average particle size

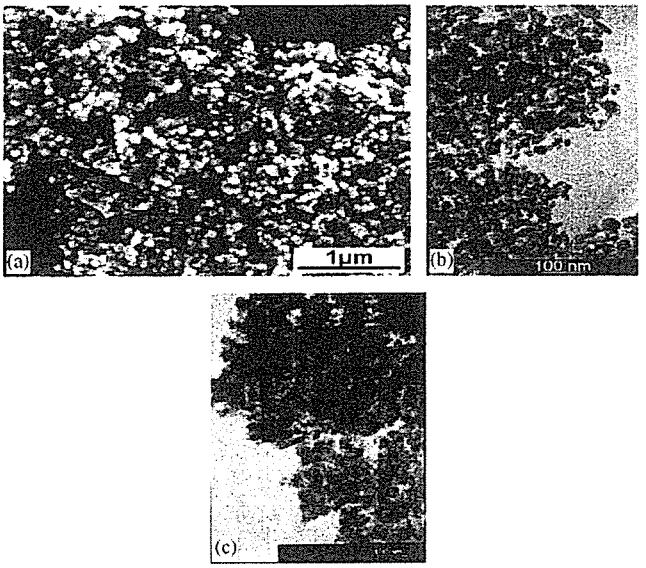

Fig. 3. (a) SEM, (b) and (c) TEM pictures showing the particle size for samples A, B, and C.

was estimated to be 80 nm by fitting the particle size distribution with a Gaussian function while it was 25 and 20 nm for sample B and C respectively, as obtained from the fitting of the particle size distribution with a lognormal function. The decrease in particle size for higher concentration of the oxidant is attributed to the faster oxidation of ferrous ion to ferric state and consequently an increase in the nucleation rate of ferrite nanoparticles. But lower molar concentrations of the oxidant result in a wide distribution of particles with larger diameter because of the varying time intervals for nucleation [27].

3.2. Magnetic properties

3.2.1. Saturation magnetization and Curie temperature

Table 1 shows the variation of saturation magnetization and coercivity of $Mn_{0.67}Zn_{0.33}Fe_2O_4$ with particle size. The saturation magnetization for the 80 nm particles is found to be 49 $A\,m^2\,kg^{-1}$ which decreases to 34 $A\,m^2\,kg^{-1}$ for the 20 nm particles. The decrease in saturation magnetization with the decrease in particle size is due to surface spin effects of small particles [28,29]. The coercivity decreases with particle size and becomes very small for the average particle size of 25 nm and below because of the presence of a considerable volume fraction of superparamagnetic particles. Fig. 4 shows the temperature dependent magnetization in a field of 800 $kA\,m^{-1}$ for the samples A, B, and C. These samples show close lying values of 632 ± 5, 627 ± 5 and 634 ± 5 K, respectively for their Curie temperature, T_c suggesting that there is no significant variation in the composition and also no size-dependent cation distribution. Similar results have been obtained by Jeyadevan et al. [23] in the case of Mn–Zn ferrite where the Curie temperature does not change with the particle size. The bulk $Mn_{0.65}Zn_{0.35}Fe_2O_4$ shows a Curie temperature [30] of

Table 1
The magnetic parameters such as saturation magnetization M_s and coercivity H_c as a function of average particle size for $Mn_{0.67}Zn_{0.33}Fe_2O_4$

KNO_3 (M)/ Ferric ion (%) concentration	Sample (Particle size in nm)	M_s ($\pm 2\,A\,m^2\,kg^{-1}$)	H_c ($\pm 0.2\,kAm^{-1}$)
0.09	A (80)	49	12.5
0.20	B (25)	39	1.5
35	C (20)	34	0.8

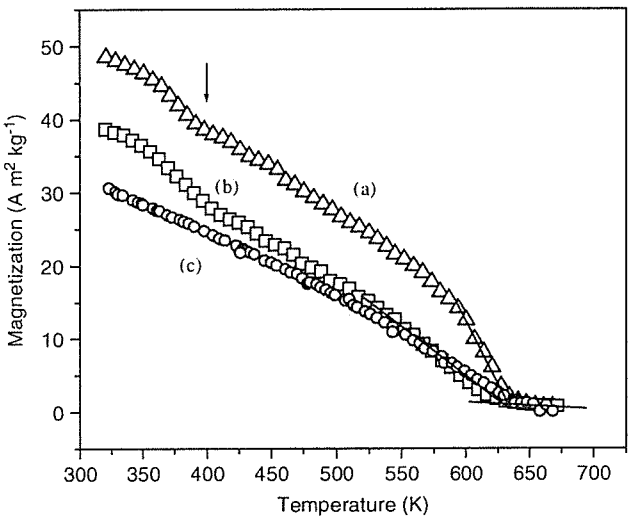

Fig. 4. The temperature-dependent magnetization of (a) sample A, (b) sample B, and (c) sample C in a magnetic field of $800\,kA\,m^{-1}$.

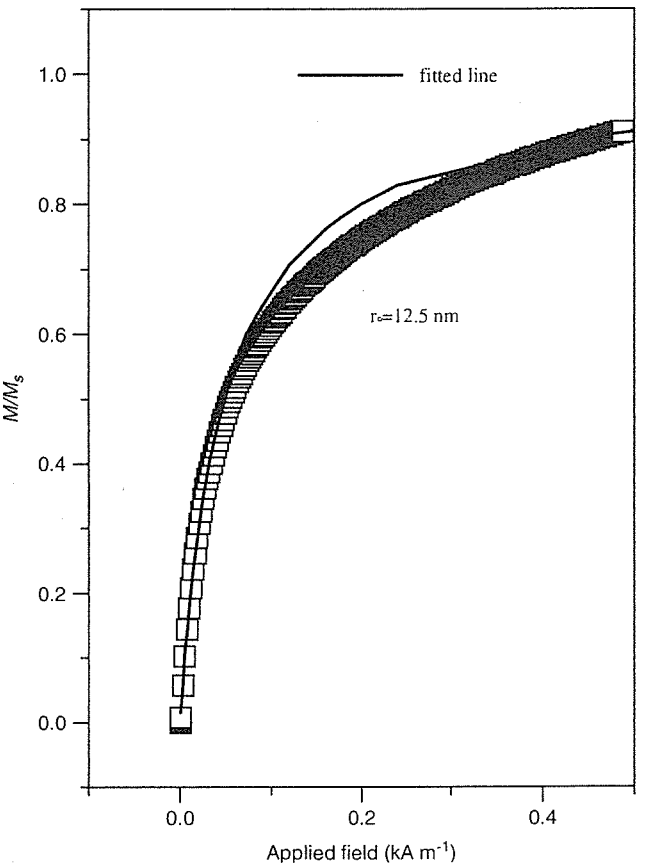

Fig. 5. The Langevin fit of the initial magnetization curve of sample B.

463 K whereas the Curie temperature of the nanoparticles of this ferrite is reported to be as high as 723 K, which is attributed to the redistribution of the cations among the two sites [4]. The cations Fe^{3+}, Mn^{2+}, and Zn^{2+} have zero crystal field stabilization energy and hence they can occupy either tetrahedral or octahedral sites randomly. Their site occupancy is found to depend on the synthesis conditions as reported in Refs. [6,10,31]. However, a few Zn^{2+} ions are found to occupy the octahedral site due to the synthesis conditions and they are shown to return to tetrahedral site on heating [32,6]. Thus the variation in cation distribution could explain the observed differences in the values of T_c reported in Refs. [4,33]. The heating during thermomagnetic measurements can facilitate cation redistribution and hence the metastable cation distribution in the as synthesized particles starts transforming to a thermally induced stable distribution as could be easily visualized from the change in the shape of the thermomagnetization curve (a), as indicated by the arrow in Fig. 4, resulting in an increase in T_c.

3.2.2. *Particle size determination from langevin function*

For an assembly of small particles exhibiting superparamagnetic behaviour, the sample magnetic moment is given by [34]

$$\frac{M(H)}{M_s} = \int_0^\infty L(\alpha)P(r)\,dr, \tag{1}$$

where M_s is the saturation magnetization, $L(\alpha)$ is the Langevin function given by $L(\alpha) = \coth(\alpha) - 1/\alpha$, $\alpha = VHM_s/k_BT$, V is the volume of the particle and the other symbols having their usual meaning, and $P(r)$ is the weight function representing the distribution in particle size. The particle size distribution is fitted with a lognormal distribution function given by

$$P(r) = \frac{1}{\sigma r\sqrt{2\pi}}\exp\left(-\ln(r/r_0)^2/2\sigma^2\right), \tag{2}$$

where σ is the standard deviation, r is the radius and r_0 is the mean radius of the particles.

The initial magnetization curve is fitted well, as seen from Fig. 5, with Eq. (1) in the low-field region using the particle size distribution function given by Eq. (2). An average particle diameter of 25 ± 1 nm was obtained from the fitting for the sample B which agrees well with the TEM results. The deviation of the Langevin fitting from the magnetization curve in the high field region is due to the surface anisotropy of small particles [35].

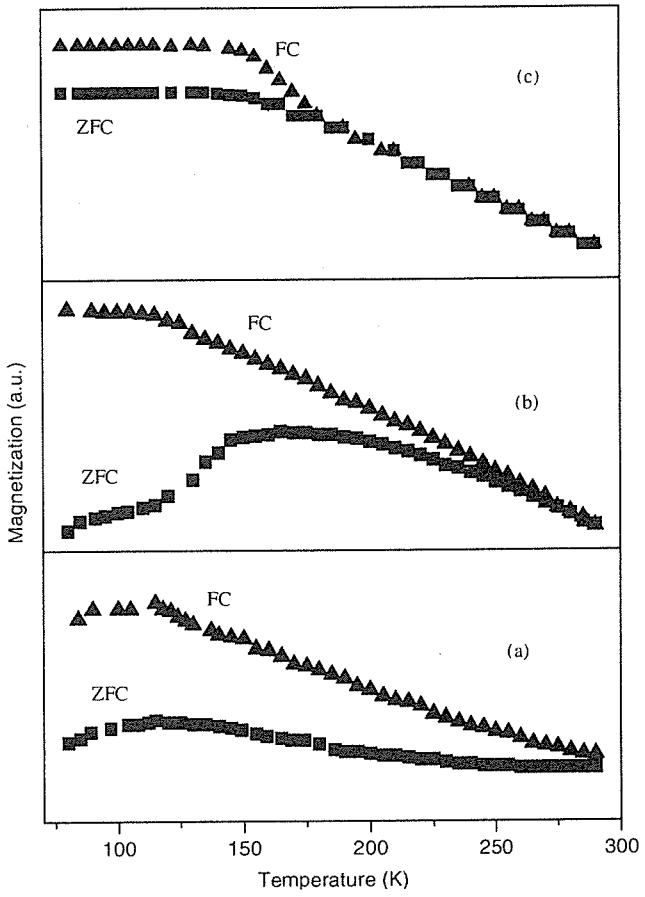

Fig. 6. The zero-field cooled and field-cooled magnetization for (a) sample A, (b) sample B, and (c) sample C in an applied field of 16 kA m^{-1}.

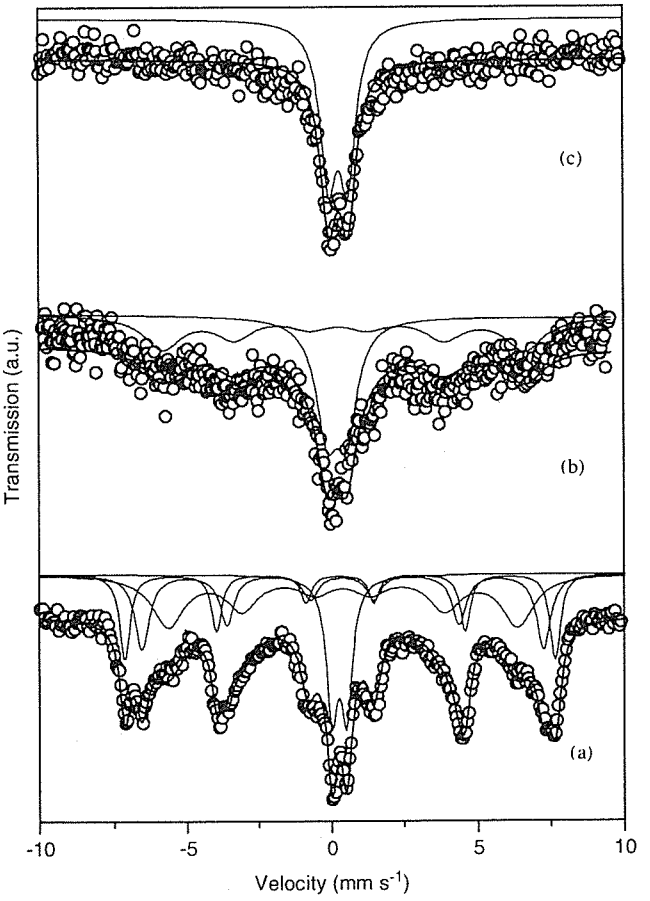

Fig. 7. The Mössbauer spectrum at 293 K for (a) sample A, (b) sample B, and (c) sample C.

3.2.3. The zero-field-cooled and field-cooled measurements

Fig. 6 shows the zero-field-cooled (ZFC) and field-cooled (FC) magnetization for samples A, B, and C, respectively in an applied magnetic field of 16 kA m^{-1}. The ZFC curve for sample C is almost flat below 135 K whereas for sample B it branches off from the FC curve at 265 K and peaks at 165 K. The large curvature in the ZFC curve for the latter suggests a broad distribution in the particle size. The large curvature in the ZFC curve for sample A compared to that observed for the other samples suggests the presence of smaller particles with a distribution in blocking temperature. The temperature at which the ZFC and FC curves separate represents the blocking temperature for larger particles [36,37]. The ZFC and FC curves for sample A do not merge together at 293 K due to the presence of a large number of bigger particles with an average particle diameter of 80 nm whose blocking temperature is expected to be above 293 K whereas for samples B and C the separation between the curves takes place at lower temperatures due to the smaller particle sizes.

3.3. Mössbauer studies

Fig. 7 shows the Mössbauer spectra at 293 K of samples A, B, and C and their corresponding Mössbauer parameters obtained from the least-squares fitting of the experimental data are shown in Table 2. The signal-to-noise ratio is poor due to relaxation effects with a wide distribution in relaxation times arising from the distribution in particle sizes of the small particles. The relaxation effects are significant if there is a distribution in particle sizes with close lying blocking temperatures [38,39]. It is significantly present in systems with low anisotropy and at temperatures above 0 K [40]. However, we could observe that a significant number of particles in samples A and B are magnetically ordered at 293 K as seen from the appearance of two sextets corresponding to the A and B sites of the spinel structure whereas all the particles in sample C are superparamagnetic at this temperature. The percentage volume of the magnetically ordered particles in sample A, as observed from the relative area of the sextet to the doublet, is 82% which decreases to 52% for sample B. The occurrence of only a superparamagnetic doublet at 293 K indicates that the blocking temperature of all the particles in sample C is below 293 K. It has been reported in Ref. [41] that the superparamagnetic limit for the Mn–Zn ferrite particles is 20 nm. The coexistence of the sextet with the superparamagnetic doublet for sample B with an average particle diameter of 25 nm and the occurrence of only a doublet for sample C with an average

Table 2
The Mössbauer parameters namely hyperfine field (H_{hf}), isomer shift (δ), quadrupole splitting (Δ), line width (Γ), and the relative intensity (I) at 293 K for samples A, B, and C

Samples (Particle size in nm)	$H_{hf} \pm 0.1$ (T)	δ [a] ± 0.05 ($mm\,s^{-1}$)	$\Delta \pm 0.06$ ($mm\,s^{-1}$)	$\Gamma \pm 0.05$ ($mm\,s^{-1}$)	$I \pm 1$ (%)
A (80)	45.8	0.39	−0.04	0.41	20
	42.8	0.48	0.02	0.58	24
	37.3	0.49	0.04	1.32	38
	—	0.38	0.51	0.47	18
B (25)	38.6	0.46	0.14	1.55	52
	—	0.31	0.68	0.88	48
C (20)	—	0.39	0.67	0.68	100

[a]Relative to α-Fe at 293 K.

particle diameter of 20 nm suggest that the particle size for the superparamagnetic limit is around 25 nm. The appearance of a broad sextet and a doublet for sample B at 293 K indicates that the blocking temperature of the particles lies near 293 K.

The hyperfine fields for the A and B sites are distinctly seen for sample A as shown by the splitting of the sextets. The largest hyperfine field with a smaller isomer shift is characteristic of Fe^{3+} ions in tetrahedral A site, whereas the other two sextets with relatively larger isomer shifts represent Fe^{3+} ions at two different environments in B-site. The A-site isomer shift is expected to be smaller than the B-site isomer shift due to a higher degree of covalency at A-site [42]. It is well known in literature that the A-site hyperfine magnetic field is greater than the B-site hyperfine field in the case of $MnFe_2O_4$ and Mn–Zn Fe_2O_4 ferrites [13,43–45]. The relative magnitudes of the hyperfine fields of two sites depend upon the type of nearest neighbours that the Fe^{3+} ions at these two sites have. A tetrahedral Fe^{3+} ion has all its twelve nearest neighbours from B-site whereas a B-site Fe^{3+} ion has six nearest neighbours from A-site and the other six from B-site itself. In Mn–Zn ferrite, Mn^{2+} and Fe^{3+} ions occupy both A- and B-sites whereas Zn^{2+} ion has a strong preference for A-site. Hence an A- site Fe^{3+} ion has more number of nearest neighbour Fe^{3+} ions from B site than a B-site Fe^{3+} ion could have. Since the Fe^{3+}(A)–O–Fe^{3+}(B) superexchange interaction strength is stronger than the Fe^{3+}(B)–O_2–Mn^{2+}(A) superexchange interaction strength and since Fe^{3+}(B)–O_2–Zn^{2+}(A) bond is nonmagnetic the superexchange interaction strength experienced by a Fe^{3+} (A) ion is greater than that by a Fe^{3+} (B) ion. This results in a higher hyperfine magnetic field at A-site than that at B-site. The A- and B-site hyperfine fields are also identified from the larger line widths and rapid fall in the hyperfine fields of B-site with temperature as mentioned in Ref. [46]. The value of 45.8 T for the hyperfine field of A-site obtained in the present study is in close agreement with the previous report [32] in the case of $Mn_{0.65}Zn_{0.35}Fe_2O_4$ nanoparticles.

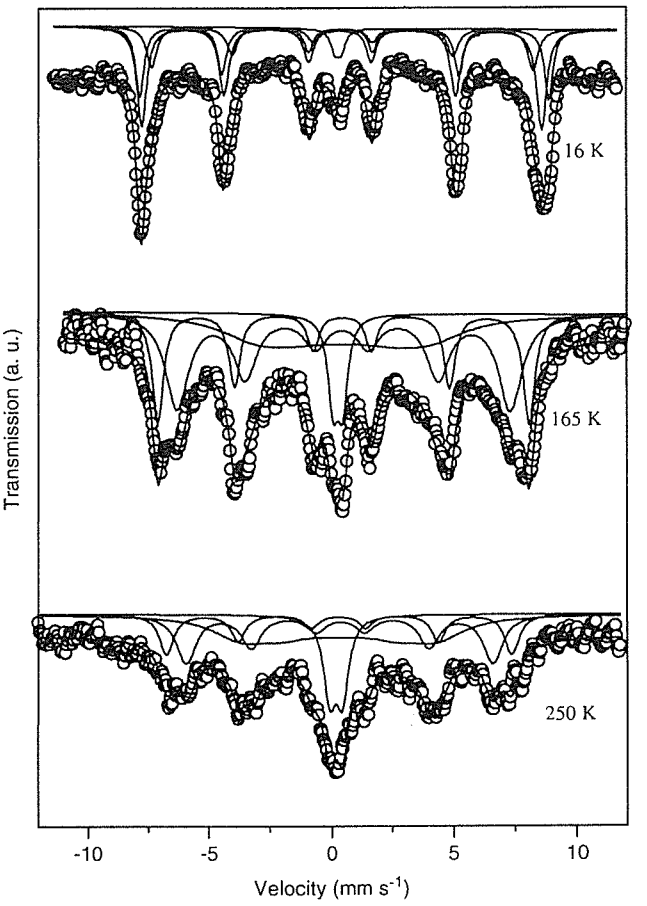

Fig. 8. The Mössbauer spectra of sample B at various temperatures.

The average value for the hyperfine fields of A- and B-sites for sample A is found to be 42 T which decreases to 38.6 T for sample B compared to the value of nearly 44 T for the bulk Mn–Zn ferrite reported in Ref. [47]. This reduction in the average hyperfine fields for the nanoparticles compared to their bulk values is due to particle size effects [48].

Fig. 8 shows the Mössbauer spectra at various temperatures for sample B. The Mössbauer spectra consist of magnetically ordered sextets along with a superparamagnetic doublet at all temperatures of measurement. The A- and B-site sextets are not well resolved due to relaxation effects in almost all spectra. But we could estimate the fraction of the magnetically ordered component from the least-squares fitting of the spectrum. The fitted Mössbauer parameters are given in Table 3. More and more particles are magnetically ordered as the temperature is lowered from 293 K. It is to be noted that partial magnetic ordering is seen for these particles even at 293 K as shown in Fig. 7(b). A superparamagnetic doublet with a small relative intensity of 6% is seen even at 16 K suggesting that a small volume fraction of particles with a blocking temperature less than 16 K is present in the sample which increases to 15% at 250 K and to 48% at 293 K. The Mössbauer spectra at 200 and 16 K for sample C are shown

Table 3
The Mössbauer parameters namely hyperfine field (H_{hf}), isomer shift (δ), quadrupole splitting (Δ), line width (Γ), and the relative intensity (I) for sample B at various temperatures

Temp. (K)	H_{hf} ±0.1 (T)	δ [a] ±0.05 ($mm\,s^{-1}$)	Δ ±0.06 ($mm\,s^{-1}$)	Γ ±0.05 ($mm\,s^{-1}$)	I ±1 (%)
250	43.7	0.41	0.01	0.70	18
	38.9	0.46	0.04	0.96	30
	24.7	0.43	0.02	2.82	37
	—	0.29	0.51	0.61	15
165	47.0	0.58	0.03	0.56	24
	42.2	0.58	−0.07	1.13	41
	21.9	0.60	0.02	3.62	27
	—	0.38	0.38	0.51	8
16	50.6	0.59	0.09	0.42	28
	48.4	0.55	−0.02	0.52	45
	44.8	0.63	0.07	0.83	21
	—	0.46	0.35	0.34	6

[a]Relative to α-Fe at 293 K.

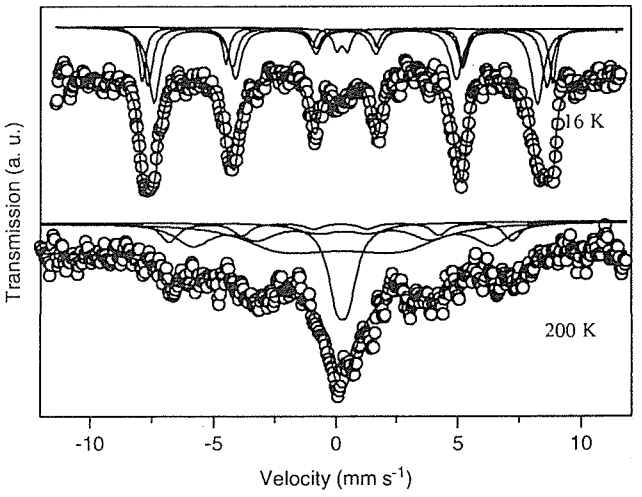

Fig. 9. The Mössbauer spectra of sample C at 200 and 16 K.

in Fig. 9. The corresponding Mössbauer parameters are given in Table 4. The low-field sextet with a large linewidth of 3.32 $mm\,s^{-1}$ at 200 K for the 20 nm particles represents the gradual transformation of the superparamagnetic doublet to a magnetically ordered sextet. This broad sextet with a low field for sample C is due to the relaxation time being nearly equal to the Mössbauer time window ($\tau \approx \tau_o$) [34]. Since the direct use of ferric ions in the synthesis has resulted in a smaller particle size compared to the samples synthesized using KNO_3, the sample C has a blocking temperature which is less than 293 K. The large line width of the sextets even at 200 K is due to relaxation effects. The large line width of the Mössbauer spectrum of this sample even at a lower temperature of 200 K compared to that of the Mössbauer spectrum of sample B at a higher temperature of 250 K is because of its smaller blocking temperature due to smaller particle size and a larger particle size distribution compared to sample B.

Table 4
The Mössbauer parameters namely hyperfine field (H_{hf}), isomer shift (δ), quadrupole splitting (Δ), line width (Γ), and the relative intensity (I) for sample C at various temperatures

Temp.(K)	H_{hf} ±0.1 (T)	δ [a] ± 0.05 ($mm\,s^{-1}$)	Δ ±0.06 ($mm\,s^{-1}$)	Γ ±0.05 ($mm\,s^{-1}$)	I ±1 (%)
200	43.3	0.32	0.01	0.87	13
	37.8	0.41	0.03	1.75	28
	17.3	0.33	0.01	3.32	39
	—	0.38	0.47	0.89	20
16	51.8	0.53	0.13	0.33	19
	50.4	0.59	0.01	0.47	30
	48.4	0.53	0.00	0.58	47
	—	0.37	0.44	0.38	4

[a]Relative to α-Fe at 293 K.

3.4. Magnetic anisotropy constant determination

The blocking temperature T_B, the temperature below which the superparamagnetic particles become magnetically ordered, is given by

$$\tau = \tau_0 e^{K_{eff} V / k_B T_B}, \quad (3)$$

where, K_{eff} is the effective magnetic anisotropy constant, V is the volume of the particle, k_B is the Boltzmann constant, τ is the relaxation time, and τ_o is the relaxation time constant. The Mössbauer measurement time scale is of the order of 10^{-8} s. If the relaxation time,τ of the nanoparticles is less than τ_o, then the thermal fluctuations make the moment fluctuate rapidly resulting in a doublet in the Mössbauer spectrum. However, the relaxation time τ increases as the temperature is lowered and at the blocking temperature, T_B the relaxation time is larger than the Mössbauer time window resulting in the appearance of a sextet. Since there is always a distribution in the relaxation times due to particle size distribution, the blocking temperature is usually taken as that temperature at which the doublet and sextet intensities are equal [49]. The T_B, therefore, as measured from the Mössbauer experiments is 293 K for sample B. Similarly T_B, from magnetic measurements (ZFC) using VSM with a measurement time of 1 s, was found to be 135 K. Using these data one could estimate the effective magnetic anisotropy constant by simultaneously solving Eq. (3), and it is found to be 7.78 $kJ\,m^{-3}$. This value is about an order of magnitude higher than the value of about 1 $kJ\,m^{-3}$ reported for the bulk Mn–Zn ferrites [50], and also is in accordance with the values reported in the literature for other nanocrystalline ferrites and this is attributed to the surface anisotropy of small particles [51]. The site occupancy of the cations also can influence the magnetocrystalline anisotropy [52].

4. Conclusion

$Mn_{0.67}Zn_{0.33}Fe_2O_4$ nanoparticles with size ranging from 80 to 20 nm have been synthesized, for the first time, using

the modified oxidation method. The 80 nm particles showed a magnetization of $49\,A\,m^2\,kg^{-1}$ at 293 K which reduced to $34\,A\,m^2\,kg^{-1}$ for the 20 nm particles. The significance of this study is that the cation distribution does not depend on the particle size as seen from the Curie temperature remaining constant independent of the particle size. The critical particle size limit for superparamagnetism is found to be 25 nm at 293 K. The larger value of $7.78\,kJ\,m^{-3}$ for the effective magnetic anisotropy constant of the 25 nm particles is attributed to the surface spin anisotropy of small particles.

Acknowledgements

One of the authors (RJJ) acknowledges the partial financial assistance under the 21st Century COE Program on Water Dynamics, Tohoku University and the CSIR, Government of India for the award of SRF. The partial financial assistance from UGC and DST, Government of India through the special assistance program and through the project No. SR/S5/NM-23/2002, respectively is acknowledged.

References

[1] Q.A. Pankhrust, J. Connolly, S.K. Jones, J. Dobson, J. Phys. D: Appl. Phys. 36 (2003) R167.
[2] V. Šepelák, U. Steinike, D.C. Uecker, S. Wißmann, K.D. Becker, J. Solid State Chem. 135 (1998) 52.
[3] C. Upadhyay, H.C. Verma, Appl. Phys. Lett. 85 (2004) 2074.
[4] C. Rath, S. Anand, R.P. Das, K.K. Sahu, S.D. Kulkarni, S.K. Date, N.C. Mishra, J. Appl. Phys. 91 (2002) 2211.
[5] A.S. Albuquerque, J.D. Ardisson, W.A.A. Macedo, M.C.M. Alves, J. Appl. Phys. 87 (2000) 4352.
[6] B. Jeyadevan, K. Tohji, K. Nakatsuka, A. Narayanasamy, J. Magn. Magn. Mater. 217 (2000) 99.
[7] T. Hyeon, Chem. Commun. 8 (2003) 927.
[8] W.J. Schuele, S. Shtrekman, D. Treves, J. Appl. Phys. 36 (1965) 1010.
[9] R.H. Kodama, A.E. Berkowitz, E.J. McNiff Jr., S. Foner, Phys. Rev. Lett. 77 (1996) 394.
[10] A. Narayanasamy, B. Jeyadevan, C.N. Chinnasamy, N. Ponpandian, J.M. Greneche, Proceedings of the Ninth International Conference on Ferrites (ICF-9), San Francisco, USA, August 2004, p. 867.
[11] C.N. Chinnasamy, A. Narayanasamy, N. Ponpandian, K. Chattopadhyay, H. Guerault, J.-M. Greneche, J. Phys. Condens. Matter. 12 (2000) 7795.
[12] L.K. Leung, B.J. Evans, A.H. Morrish, Phys. Rev. B 8 (1973) 29.
[13] G.A. Sawatzky, F. van der Woude, A.H. Morrish, Phys. Rev. 187 (1969) 747.
[14] H.H. Hamdeh, W.M. Hikal, S.M. Taher, J.C. Ho, N.P. Thuy, O.K. Quy, N. Hanh, J. Appl. Phys. 97 (2005) 64310.
[15] C. Upadhyay, H.C. Verma, C. Rath, K.K. Sahu, S. Anand, R.P. Das, N.C. Mishra, J. Alloys. Compds. 326 (2001) 94.
[16] K. Mandal, S. Chakraverty, S.P. Mandal, P. Agudo, M. Pal, D. Chankravorty, J. Appl. Phys. 92 (2002) 501.
[17] T. Sato, T. Ijima, M. Seki, N. Inagaki, J. Magn. Magn. Mater. 65 (1987) 252.
[18] C. Liu, B. Zou, A.J. Rondinone, Z.J. Zhang, J. Am. Chem. Soc. 122 (2000) 6263.
[19] A.F. Bakuzis, P.C. Morais, F. Pelegrini, J. Appl. Phys. 85 (1999) 7480.
[20] L.D. Tung, V. Kolesnichenko, D. Caruntu, N.H. Chou, C.J. O'Connor, L. Spinu, J. Appl. Phys. 93 (2003) 7486.
[21] C.N. Chinnasamy, M. Senuoue, B. Jeyadevan, O. Perales-Peres, K. Shinoda, K. Tohji, J. Colloid Interface Sci. 263 (2003) 80.
[22] C.N. Chinnasamy, B. Jeyadevan, K. Shinoda, K. Tohji, D.J. Djayaprawira, M. Takahashi, R. Justin Joseyphus, A. Narayanasamy, Appl. Phys. Lett. 83 (2003) 2862.
[23] B. Jeyadevan, C.N. Chinnasamy, K. Shinoda, K. Tohji, H. Oka, J. Appl. Phys. 93 (2003) 8450.
[24] H. Tamura, E. Matijevic, J. Colloid Interface Sci. 90 (1982) 100.
[25] K. Nishimura, M. Abe, M. Inoue, IEEE Trans. Magn. 38 (2002) 3222.
[26] C. Rath, K.K. Sahu, S. Anand, S.K. Date, N.C. Mishra, R.P. Das, J. Magn. Magn. Mater. 202 (1999) 77.
[27] V.K. LaMer, R.H. Dinegar, J. Am. Chem. Soc. 72 (1950) 4847.
[28] J.M.D. Coey, Phys. Rev. Lett. 27 (1971) 1140.
[29] R.H. Kodama, A.E. Berkowitz, Phys. Rev. B 59 (1999) 6321.
[30] J. Smith, H.P.J. Wijn, Ferrites, Wiley, New York, 1959, p.369.
[31] K. Tkácová, V. Šepelák, N. Števulová, V.V. Boldyrev, J. Solid State Chem. 123 (1996) 100.
[32] C. Rath, N.C. Mishra, S. Anand, R.P. Das, K.K. Sahu, C. Upadhyay, H.C. Verma, Appl. Phys. Lett. 76 (2000) 475.
[33] S. Son, R. Swaminathan, M.E. McHenry, J. Appl. Phys. 93 (2003) 7495.
[34] S.A. Oliver, R.J. Willey, H.H. Hamdeh, G.O. Busca, Scr. Metall. Mater. 33 (1995) 1695.
[35] M. Respaud, J. Appl. Phys. 86 (1999) 556.
[36] M.F. Hansen, S. Mørup, J. Magn. Magn. Mater. 203 (1999) 214.
[37] C. Cannas, M.F. Casula, G. Concas, A. Corrias, D. Gatteschi, A. Falqui, A. Musinu, C. Sangregorio, G. Spano, J. Mater. Chem. 11 (2001) 3180.
[38] W.J. Schuele, S. Shtrikman, D. Treves, J. Appl. Phys. 36 (1965) 1010.
[39] J.L. Dormann, F. D'Orazio, F. Lucari, E. Tronc, P. Prené, J.P. Jolivet, D. Fiorani, Phys. Rev. B 53 (1996) 14291.
[40] C.M. Srivastava, S.N. Shringi, R.G. Srivastava, Phys. Rev. B 14 (1976) 2041.
[41] K. Mandal, S. Chakraverty, S.P. Mandal, P. Agudo, M. Pal, D. Chankravorty, J. Appl. Phys. 92 (2002) 501.
[42] N.N. Greenwood, T.C. Gibb, Mössbauer spectroscopy, Chapman & Hall, London, 1971 (Sec. 10).
[43] R.G. Gupta, R.G. Mendiratta, J. Appl. Phys. 48 (1977) 845.
[44] M. Arshed, N.M. Butt, M. Siddique, M. Anwar-ul-Islam, T. Abbas, M. Ahmed, Solid State Commun 84 (1992) 717.
[45] T. Kanazaki, K. Kikuchi, M. Sato, K. Nagai, T. Oowada, H. Onozuka, K. Kitayama, J. Electron Spectrosc. Relat. Phenom. 77 (1996) 221.
[46] K. Krieble, T. Schaeffer, J.A. Paulsen, A.P. Ring, C.C.H. Lo, J.E. Snyder, J. Appl. Phys. 97 (2005) 10F101.
[47] L. Cser, I. Deszi, I. Gladkih, L. Keszthelyi, D. Kulgawcsuk, N.A. Eissa, E. Sterk, Phys. Stat. Sol. 27 (1968) 131.
[48] J.Z. Jiang, G.F. Goya, H.R. Rechenberg, J. Phys. Condens. Matter. 11 (1999) 4063.
[49] A.J. Rondinone, A.C.S. Samia, Z.J. Zhang, Appl. Phys. Lett. 76 (2000) 3624.
[50] S. Chikazumi, Physics of Magnetism, Wiley, New York, 1964, p.141.
[51] B. Martínez, A. Roig, E. Molins, T. González-Carreño, C.J. Serna, J. Appl. Phys. 83 (1998) 3256.
[52] C.N. Chinnasamy, A. Narayanasamy, N. Ponpandian, K. Chattopadhyay, K. Shinoda, B. Jeyadevan, K. Tohji, K. Nakatsuka, T. Furubayashi, I. Nakatani, Phys. Rev. B 63 (2001) 184108.

Available online at www.sciencedirect.com
SCIENCE DIRECT®
Chemical Physics Letters 417 (2006) 288–292
CHEMICAL PHYSICS LETTERS
www.elsevier.com/locate/cplett

Electrically triggered insertion of single-stranded DNA into single-walled carbon nanotubes

Takeru Okada [a,*], Toshiro Kaneko [a], Rikizo Hatakeyama [a], Kazuyuki Tohji [b]

[a] *Department of Electronic Engineering, Tohoku University, 6-6-05 Aramaki-Aza, Aoba-ku, Sendai, Miyagi 980-8579, Japan*
[b] *Graduate School of Environmental Studies, Tohoku University, Sendai 980-8579, Japan*

Received 8 June 2005; in final form 3 October 2005
Available online 2 November 2005

Abstract

The formation of DNA encapsulated carbon nanotubes, which are expected to modify electronic properties of carbon nanotubes, is for the first time demonstrated using a modified electrophoresis method. Radio-frequency and direct-current electric fields are applied to the DNA solution in order to stretch random-coil-shaped DNA and irradiate DNA to carbon nanotubes that are coated onto electrodes immersed in the DNA solution, respectively. Transmission electron microscopy and Raman scattering spectroscopy analyses reveal that DNA can be encapsulated into the carbon nanotubes. In this procedure, the key for the formation of DNA encapsulated carbon nanotubes is found to irradiate the stretched-shaped DNA to the carbon nanotubes.
© 2005 Elsevier B.V. All rights reserved.

1. Introduction

Much attention and a variety of studies have been devoted to electronic, chemical, and physical modifications of single-walled carbon nanotubes (SWNTs). The modification modes of SWNTs are roughly divided into two approaches. One is intercalation of materials between bundles [1–3] or attachment to outside walls of SWNTs [4–6]. The other is encapsulation of materials in the inside of SWNTs [7–12]. Intercalation can modify electronic properties of SWNTs, which does not require so complicated procedure in general. However, intercalation is inevitably beset with problems for future applications, for example, air-stability of the intercalated SWNTs is one of the most fatal issues for the realization of novel electronic devices because the intercalated functional materials are exposed to the air. On the contrary, functional-material encapsulated SWNTs are expected to ensure this air stability, because the functional materials are inserted inside the hollow regions of SWNTs and are isolated from the air. Although the alkali metal [13], C_{60} [14], and organic molecules [12] have been used as the encapsulated functional materials so far, DNA is also an interesting material for the future applications not only in biology but also other fields because of their unique properties. DNA consists of four kinds of bases, each of which has a different electronic property [15], and the base sequence has come to be easily controlled in recent years.

To the best of our knowledge, there have been some papers which relate to the combination between SWNTs and DNA [16,17]. However, the approaches of the papers are limited to the utilization of outside wall of SWNTs. On the contrary, our viewpoint is focused upon the utilization of inside nano-space of SWNTs innovating DNA. Thus, DNA is expected to reflect its electronic properties in characterizing SWNTs when DNA is encapsulated into SWNTs. As a result, encapsulated DNA is predicted to modify electronic properties of the SWNTs in accordance with changing length and base sequence of DNA. Here, we demonstrate for the first time the formation of DNA encapsulated SWNTs (DNA@SWNTs) that are expected to yield great potential for nano-scale electronics.

* Corresponding author. Fax: +81 22 263 9225.
E-mail address: okada@ecei.tohoku.ac.jp (T. Okada).

0009-2614/$ - see front matter © 2005 Elsevier B.V. All rights reserved.
doi:10.1016/j.cplett.2005.10.030

2. Experimental

In this study, SWNTs are purified in advance, which were produced by an arc discharge method [18]. After purification, SWNTs are treated by heat for the opening of SWNTs tips. The heat treatment is performed in the air for 30 min at 750 K. The formation of open-ended SWNTs is confirmed by the formation of C_{60} encapsulated SWNTs in the same way as reported by Bandow et al. [9]. The purity of SWNTs remains high even after heat treatment for the opening of the tip. The peak intensity ratio of G band to D band (G/D ratio) in Raman spectra of SWNTs after heat treatment is more than 50 when excitation energy of laser is 2.54 eV. The average diameter of SWNTs is about 1.5 nm and the diameter is distributed in the rage of 1.2–1.7 nm. We adopt two kinds of single-stranded DNA (ssDNA) with different lengths as a material for the insertion into SWNTs. One ssDNA consists of 15 adenines (15A-DNA) and the other consists of 30 adenines (30A-DNA). Since the length of 10 bases is estimated to be 3.4 nm on the assumption that DNA molecules make up a helix conformation, the lengths of 15A-DNA and 30A-DNA are about 5 and 10 nm, respectively.

Fig. 1 shows schematic of an experimental apparatus to irradiate ssDNA which is dissolved into water to open-ended SWNTs. Open-ended SWNTs are coated onto aluminum electrodes (anode and cathode) which are submerged in the ssDNA solution. The distance of the two electrodes is 1 mm and the volume of the ssDNA solution is 5 ml. When a direct current (DC) bias voltage (V_{DC}) is applied to the anode electrode, ssDNA is considered to be irradiated to it in the same way as an electrophoresis

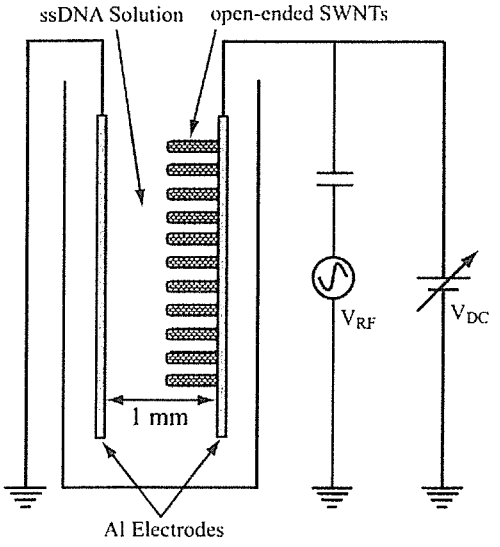

Fig. 1. Schematic of an experimental apparatus for the formation of DNA encapsulated carbon nanotubes, where both the DC and RF electric fields can independently be applied to the ssDNA solution. Open-ended SWNTs are considered to be oriented perpendicularly to the anode electrode along the electric field, which is formed by applying the DC and/or RF voltages to the electrodes.

method because DNA molecules constitute the phosphoric acid group which has a negative charge. Since DNA molecules make up the random-coiled conformation in solution, however, it is difficult to encapsulate DNA molecules directly into SWNTs. When an radio frequency (RF) electric field is externally applied to DNA, on the other hand, dominant dipole moment is induced along DNA axis because of their high anisotropicity, resulting in stretching DNA molecules parallel to the external electric field due to the interaction between the external field and the induced dipole. In addition, this kind of ponderomotive force [19] generated by the RF electric field is supposed to work on moving the stretched and orientated DNA molecules to both the anode and the cathode. Thus, we superimpose the radio frequency voltage (V_{RF}) upon V_{DC} in order to stretch DNA molecules and irradiate them to the electrodes, as given in Fig. 1 [20,21]. Furthermore, in the case that the DC and/or RF electric fields are applied, SWNTs are considered to stand on the electrodes along the electric fields and the orientation of the SWNTs is expected to be perpendicular to the electrodes [14,19].

3. Results and discussion

After the irradiation of the DNA molecules to the electrodes, they are adsorbed onto the aluminum surface of the electrodes and the adsorption is maintained semipermanently [15]. Furthermore, the aggregation of ssDNA is initiated at the aluminum surface by the existence of the aluminum ions coming from the V_{DC} and/or V_{RF} applied electrodes. Therefore, the amount of the irradiated DNA molecules to the anode–electrode surface can be estimated by measuring the concentration of the DNA solution after applying V_{DC} and/or V_{RF}. Here, UV–vis absorption spectra of the DNA solution are available for calculating the DNA concentration.

Fig. 2a presents a typical UV–vis absorption spectrum of the ssDNA solution, where we can find a specific absorption peak around 260 nm originating from the DNA molecules. Then, the concentration of the solution is obtained using the peak intensity dependence under the normalization that the value of 1 in absorbance corresponds to about 35 μg/ml. The time evolution of the calculated concentration of the DNA solution with V_{DC} as a parameter is plotted in Fig. 2b, where the concentration decreases with the irradiation time and an increase in V_{DC}. The results indicate that the DNA irradiation is controlled by changing the DC bias voltage and irradiation time. In the case of $V_{DC} = 10$ V, almost all of the DNA molecules appear to be irradiated to the anode. Based on the DNA-concentration results, the irradiation of DNA to the open-ended SWNTs to form the DNA encapsulated SWNTs is performed within 10 min for $V_{DC} = 10$ V in the following measurements.

Fig. 3 shows spectra of Raman scattering spectroscopy in the range of the radial breathing mode of SWNTs, which are measured by using different laser excitation energies (a)

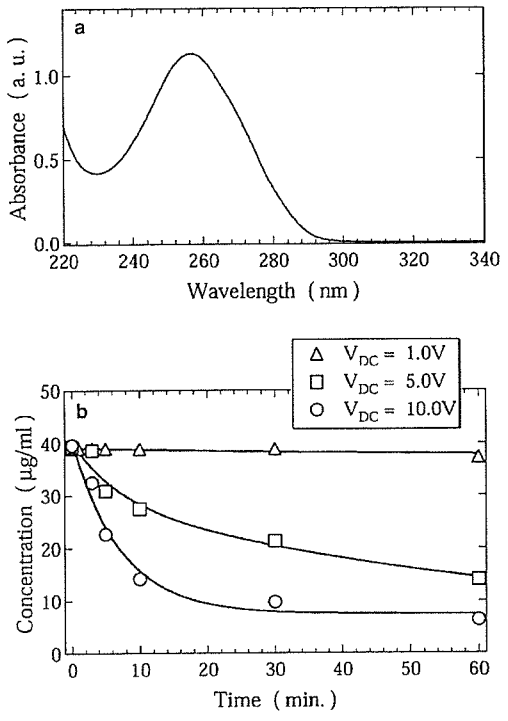

Fig. 2. (a) Typical UV–vis absorption spectrum of ssDNA solution. (b) Time evolution of the concentration of ssDNA solution with V_{DC} as a parameter.

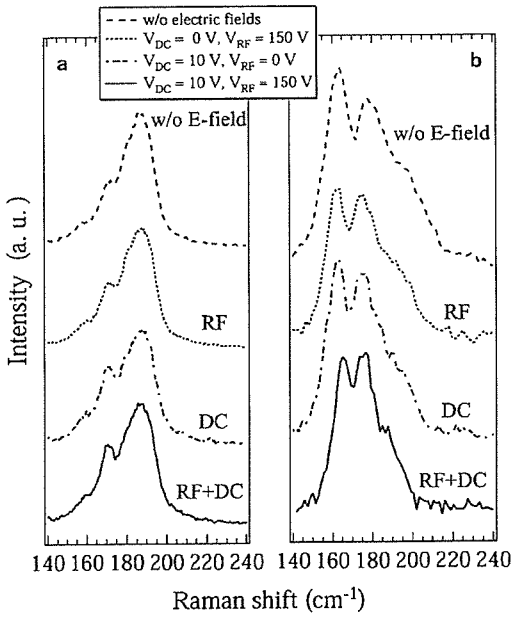

Fig. 3. Raman spectra of SWNTs after ssDNA (15A-DNA) irradiation. Excitation energies of laser are (a) 2.41 eV and (b) 2.54 eV, respectively.

2.41 eV and (b) 2.54 eV. The Raman spectra of SWNTs after the ssDNA irradiation are obtained under the dried condition after the removal of DNA attached on the surface of SWNTs by washing with water. The shape of the spectra and the peak intensity are found to be different between the cases with and without applying electric fields, especially in the case of the excitation energy of 2.54 eV. The changes of the peak intensity in the range of the radial breathing mode (RBM) are considered to be one of the phenomena associated with charge transfer between ssDNA and carbon nanotubes. Although the effect of charge transfer may be very small, the signal of RBM is considered to be very sensitive to the condition of the SWNT inner region. As a result, even a slight effect of the charge transfer has the possibility of changing RBM, giving indirect evidence of the encapsulation of other materials inside SWNTs.

When only the DC electric field is applied (DC), the spectra shapes become sharp (Fig. 3a, b) and the intensity ratio of two peaks observed in Fig. 3b is changed compared with the case where no electric field is applied (w/o E-field). Since the DC electric field is predicted to induce the driving force enhancing the insertion of the DNA molecules as described above, such features in the Raman spectra are due to the effect of the DNA irradiation triggered by the DC field application. According to observations by high-resolution transmission electron microscopy (HR-TEM), however, the yield of DNA@SWNTs seems to be not so high under this condition.

On the other hand, an appreciable difference is recognized between the cases with and without RF electric field applied SWNTs (RF). In this situation, a part of 15A-DNA can be stretched by the RF electric field and inserted into SWNTs even in the absence of strong external driven force such as a DC electric field, because the length of 15A-DNA is about 5 nm and its diameter is comparatively similar to the diameter of SWNTs (1.2–1.7 nm). It is plausible that ssDNA can be inserted to some extent into opened-SWNTs without the positive DNA irradiation, which is not inconsistent with a simulation study reported by Gao et al. [22]. Based on the Raman analyses, however, the yield is estimated to be quite low when only the RF electric field is applied in the absence of the DC electric field.

Furthermore, in the case that both V_{DC} and V_{RF} are applied simultaneously, in other words, stretched ssDNA is irradiated (RF + DC), the spectrum shape becomes sharper, for example, a hump around 185 cm^{-1} in Fig. 3b disappears. In addition, we can perceive some changes in the peak intensities around 180 cm^{-1} in Fig. 3a and at 164 and 178 cm^{-1} in Fig. 3b. These results imply that the encapsulation yield of ssDNA into open-ended SWNTs is considerably enhanced when both the DC and RF electric fields are superimposed.

Based on the results in Fig. 3, the rate of encapsulation of ssDNA into SWNTs is considered to be estimated with a decrease in the peak intensity at 164 cm^{-1} compared with the peak intensity at 178 cm^{-1}. The ratio of peak intensity at 164 cm^{-1} to that at 178 cm^{-1} in the Raman spectrum is plotted as a function of V_{DC} for $V_{RF} = 50$ V in Fig. 4, where laser excitation energy is 2.54 eV. The ratio decreases with an increase in the applied DC electric field. As already shown in Fig. 2, the amount of irradiation of DNA nega-

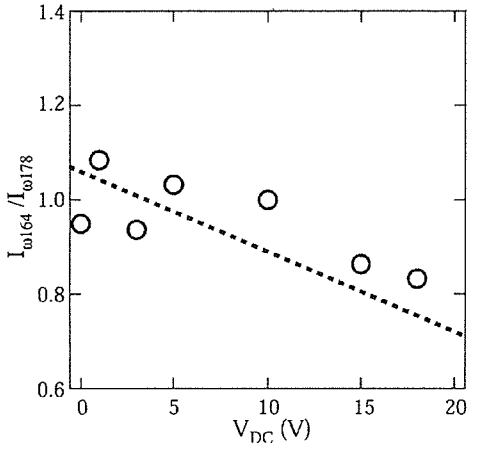

Fig. 4. The peak intensity ratio of 164–178 cm^{-1} in Raman spectra of SWNTs after ssDNA irradiation as a function of V_{DC} for $V_{RF} = 50$ V. Laser excitation energy is 2.54 eV.

tive ions is found to depend on the applied DC electric field. Thus, when the conformation of DNA is stretched by the RF electric field, the encapsulation ratio resultantly depends on the DNA ion irradiation. Therefore, the large amount of stretch-shaped ssDNA irradiation leads to the improvement of the yield of DNA@SWNTs.

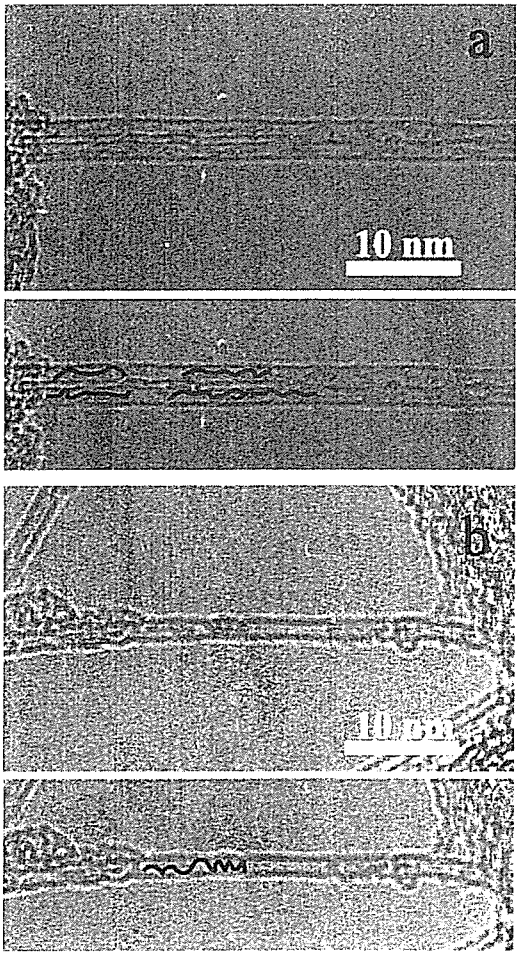

Fig. 5. HR-TEM images of SWNTs after ssDNA irradiation in the cases of using (a) 15A-DNA (about 5 nm lengths) and (b) 30A-DNA (about 10 nm lengths). The black lines in images indicate encapsulated materials.

The intensive observation of SWNTs undergoing the DNA irradiation is performed using HR-TEM, where the acceleration voltage is 200 kV. Fig. 5a presents HR-TEM images of SWNTs after the DNA irradiation under the condition of $V_{DC} = 10$ V and $V_{RF} = 20$ V in the case of 15A-DNA. The one-dimensional materials appear to be encapsulated in SWNTs, where the black lines in the images indicate the encapsulated materials. The length of the encapsulated material is about 5 nm which corresponds to that of 15A-DNA. In the case of using 30A-DNA, the HR-TEM image is shown in Fig. 5b, where the DNA irradiation condition is $V_{DC} = 10$ V and $V_{RF} = 150$ V. The encapsulated material is also observed and its length is estimated to be about 10 nm. Besides, 30A-DNA is found to form a helical conformation inside SWNTs and seems to be adsorbed onto the inner wall. Based on the TEM observation, it is likely that the bases, hydrophobic part of DNA, and the certain length of ssDNA tend to be adsorbed onto the inner wall and to form the helical conformation in SWNTs, respectively [23].

Since the ssDNA irradiation method described here utilizes negatively charged part of ssDNA molecules, i.e., phosphoric acid group in the ssDNA molecules and the stretch of ssDNA molecules is caused by the interaction of the permittivity of ssDNA with applied external electric fields, the effect of irradiation and stretch is independent of the base sequence. Therefore, this formation method of DNA encapsulated SWNTs can be applied to not only specific base sequence of DNA consisting of, for example, only adenines, but also any base sequence.

4. Summary

In conclusion, the ssDNA encapsulated SWNTs are created for the first time by applying DC and RF electric fields to the DNA solution. Based on the Raman spectrum and HR-TEM analyses, the encapsulation of ssDNA into open-ended SWNTs is enhanced when both the DC and RF electric fields are simultaneously superimposed. It is found that ssDNA is adsorbed onto the inner wall of SWNTs and exists in the form of helical conformation when the length of ssDNA is enough decisive. These results lead to a claim that a process of superimposing RF electric field upon DC electric field plays a decisive role in the DNA encapsulated SWNT formation in this solution-phase procedure. The ssDNA encapsulated SWNTs could have a possibility of novel electrical modification of SWNTs.

Acknowledgments

The authors thank Dr. Y. Sato and Mr. K. Motomiya for their technical support. This research was partly carried out at the Laboratory for Nanoelectronics and Spintronics,

Research Institute of Electrical Communication, Tohoku University. Part of this work was carried out under the Cooperative Research Project Program of the Research Institute of Electrical Communication, Tohoku University. This work was also supported by a Grant-in-Aid for Scientific Research from the Ministry of Education, Culture, Sports, Science and Technology, Japan, and Tohoku University 21st COE (Center of Excellence) Program.

References

[1] R.S. Lee, H.J. Kim, J.E. Fischer, A. Thess, R.E. Smalley, Nature 388 (1997) 255.
[2] A.M. Rao, P.C. Eklund, S. Bandow, A. Thess, R.E. Smalley, Nature 388 (1997) 257.
[3] J. Kong, C. Zhou, E. Yenilmez, H. Dai, Appl. Phys. Lett. 77 (2000) 3977.
[4] S.E. Baker, W. Cai, T.L. Lasseter, K.P. Weidkamp, R.J. Hamers, Nano Lett. 2 (2002) 1413.
[5] K.A. Williams, P.T.M. Veenhuizen, B.G. de la Torre, R. Eritja, C. Dekker, Nature 420 (2002) 761.
[6] H. Cai, X. Cao, Y. Jiang, P. He, Y. Fang, Anal. Bioanal. Chem. 375 (2003) 287.
[7] R. Hatakeyama, T. Hirata, G.-H. Jeong, Plasma Source Sci. Technol. 13 (2004) 108.
[8] S. Bandow, M. Takizawa, H. Kato, T. Okazaki, H. Shinohara, S. Iijima, Chem. Phys. Lett. 347 (2001) 23.
[9] S. Bandow, M. Takizawa, H. Hirahara, M. Yudasaka, S. Iijima, Chem. Phys. Lett. 337 (2001) 48.
[10] H. Kataura, Y. Maniwa, T. Kodama, K. Kikuchi, K. Hirahara, K. Suenaga, S. Iijima, S. Suzuki, Y. Achiba, W. Kratschmer, Synth. Met. 121 (2001) 1195.
[11] R. Pfeiffer, H. Kuzmany, W. Plank, T. Pichler, H. Kataura, Y. Achiba, Diam. Relat. Mater. 11 (2002) 957.
[12] T. Takenobu, T. Takano, M. Shiraishi, Y. Murakami, M. Ata, H. Kataura, Y. Achiba, Y. Iwasa, Nature Mater. 2 (2003) 683.
[13] G.-H. Jeong, A.A. Frajian, R. Hatakeyama, T. Hirata, T. Yaguchi, K. Tohji, H. Mizuseki, Y. Kawazoe, Phys. Rev. B 68 (2003) 075410.
[14] G.-H. Jeong, T. Hirata, R. Hatakeyama, K. Tohji, K. Motomiya, Carbon 40 (2002) 2247.
[15] K.-H. Yoo, D.H. Ha, J.-O. Lee, J.W. Park, J. Kim, J.J. Kim, H.-Y. Lee, T. Kawai, H.-Y. Choi, Phys. Rev. Lett. 87 (2001) 198102.
[16] N. Nakashima, S. Okuzono, H. Murakami, T. Nakai, K. Yoshikawa, Chem. Lett. 32 (2003) 456.
[17] M. Zheng, A. Jagota, E.D. Semke, B.A. Diner, R.S. Mclean, S.R. Lusting, R.E. Richardson, N.G. Tassi, Nature Mater. 2 (2003) 338.
[18] K. Tohji, T. Goto, H. Takahashi, Y. Shinoda, N. Shimizu, B. Jeyadevan, I. Matsuoka, Y. Saito, A. Kasuya, T. Ohsuna, K. Hiraga, Y. Nishina, Nature 383 (1996) 679.
[19] R. Krupke, F. Hennrich, H.B. Weber, M.M. Kappes, H.V. Lohneysen, Nano Lett. 3 (2003) 1019.
[20] M. Washizu, O. Kurosawa, IEEE Trans. Ind. Appl. 26 (1990) 1165.
[21] S. Suzuki, T. Yamanashi, S. Tazawa, O. Kurosawa, M. Washizu, IEEE Trans. Ind. Appl. 34 (1998) 75.
[22] H. Gao, Y. Kong, D. Cui, C.S. Ozakan, Nano Lett. 3 (2003) 471.
[23] M. Zheng, A. Jagota, M.S. Strano, A.P. Santos, P. Barone, S.G. Chou, B.A. Diner, M.S. Dresselhaus, R.S. Mclean, G.B. Onoa, G.G. Samsonidze, E.D. Semke, M. Usrey, D.J. Walls, Science 302 (2003) 1545.

Available online at www.sciencedirect.com
ScienceDirect
Materials Letters 60 (2006) 3041 – 3044
materials letters
www.elsevier.com/locate/matlet

Hydrothermal formation of diamond from chlorinated organic compounds

Sergiy Korablov *, Kazunori Yokosawa, Dmytro Korablov, Kazuyuki Tohji, Nakamichi Yamasaki

Tohoku University, Department of Environmental Studies, Graduate School of Environmental Studies, Aramaki, Aoba ku, Sendai 980-8579 Japan

Received 30 June 2004; accepted 17 July 2005
Available online 3 March 2006

Abstract

The unique properties of diamond are well known a long time ago and therefore are extensively used. However, the most general aspects of diamond origin are not yet clearly determined. Hydrothermal synthesis as any heterogeneous reactions occurring under the conditions of high-temperature–high-pressure (> 100 °C, > 1 atm) in aqueous solutions in closed system has a growing interest among the scientists in particular due to a possibility of synthesis of new phases or crystals growth. During this study the diamond particles or films were produced through hydrothermal interaction of 1,1,1-Trichloroethane and 10 M NaOH in the presence of diamond or cubic BN seeds at temperature 300 °C and pressure 1 GPa. Synthesized diamond was thoroughly characterized by TG–DTA, SEM (EDX) and had (220) preferable orientation according to XRD pattern. These results demonstrate that the hydrothermal growth of diamond in like manner with quarts and emerald is possible.
© 2006 Elsevier B.V. All rights reserved.

Keywords: Amorphous carbon; Diamond film; Cubic BN; Diamond

1. Introduction

At present diamond is effectively produced by melt (HPHT) [1], gas (CVD) [2] and shock-wave [3]. However, the question about natural diamond genesis is still debated and the accumulation knowledge in alternative methods of diamond growth is continued. Recently some attempts to overcome the limitations of usual synthesis methods through radically different processes, for example, rapid nonhydrostatic compression of C_{60} at room temperature [4], extracting silicon from silicon carbide in chlorine-containing gases at ambient pressure [5], selective leaching of silicon carbide by high-pressure, high-temperature water [6] have been done. A review of liquid phase systems pertinent to diamond synthesis was adduced [7] and hydrothermal synthesis of diamond by low-pressure [8,9] and high-pressure [10] liquid phase epitaxy on seeds was presented. Hydrothermal growth of diamond in metal–C–H_2O system was achieved [11]. However, as fairly noted [12] for both [8,11], the problem is proving that there is a new growth of diamond in the presence of diamond seeds. Here we report that diamond structured carbon has been synthesized through namely hydrothermal reaction of liquid according to P–T conditions [13] reagents: 1,1,1-Trichloroethane and 10 M NaOH solution in the presence of hydrogenated natural diamond or cubic BN seeds at 300 °C and 1 GPa pressure without any catalyst metals.

2. Experimental details

Hydrothermal reaction has been fulfilled in piston-cylinder device [14]. Two types of copper container 0.6 and 7 ml volume were used in our experiments. Natural diamond powder 5000 and 325# (Osaka Diamond Industrial Co., Ltd.) have been firstly hydrogenated similarly to Ref. [15] while 325# cubic BN (Sumitomo Electric Industries Ltd.) was preliminary treated in H_2 plasma.

Our approach was to conduct hydrothermal reaction at the certain artificially created surfaces. So, several pellets containing 2 g/cm^3 of 5000# or 4 g/cm^3 of 325# diamond seeds have been prepared after mixing with Cu powder (Wako Pure Chemical Industries, Ltd.) by pressuring in steel mold at 150 MPa load. In contrast with free seeds in the case of fixed ones the new growth can easily pass only on the surface of pellets preferably as film.

Hydrogenated (h-diamond) powder and/or Cu-combined seeds were placed on the bottom of copper container with liquid reagents 1,1,1-Trichloroethane ($C_2H_3Cl_3$) and 10 M NaOH both (Wako Pure Chemical Industries, Ltd.) in proportion 1 : 2. Then sealed copper container was loaded up to 1 GPa in piston-

* Corresponding author.

0167-577X/$ - see front matter © 2006 Elsevier B.V. All rights reserved.
doi:10.1016/j.matlet.2005.07.092

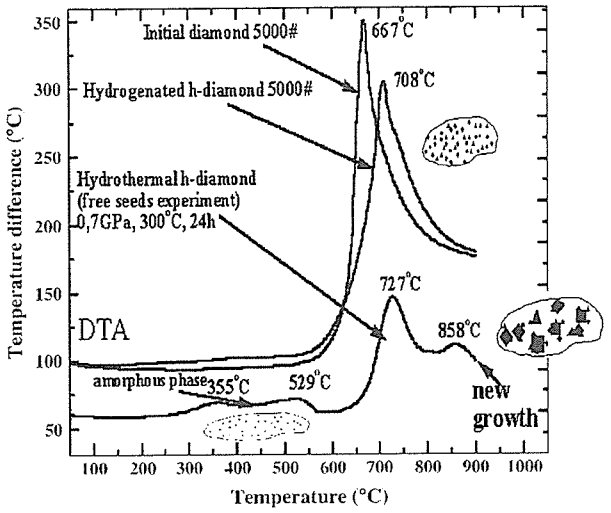

Fig. 1. DTA curves of non-isothermal oxidation in air with heating rate 10°/min. Hydrothermal h-diamond was firstly subjected to two steps acid treatment.

cylinder type high-pressure vessel and slowly heated up to 300 °C with different heating rates (0.1–1.2°/min). After 1–3 days exposure the reaction products have been extracted, ultrasonic cleaned in distilled water and acetone. Then two steps of acid treatment were applied. Firstly ballast products NaCl, $CuCl_2 \cdot Cu(OH)_2$, NaCuO were eliminated after treatment in Aqua regia during 24 h at room temperature.

3. Results and discussion

Hydrothermal conditions are far from equilibrium for diamond growth, therefore some non-diamond carbon naturally appears. For example, in the experiments without diamond seeds we found only amorphous carbon, no other carbon forms regardless of different organic precursors. For effective removing of amorphous carbon we used two approaches. One is boiling in mixture of sulfuric acid and $K_2Cr_2O_7$ during 2–4 h. Another is elimination of surface non-diamond carbon by oxidation in air.

After two steps of acid treatment (experiment with free seeds) the reaction products had white color and did not reveal any differences in X-ray diffraction (XRD) and Raman shift data in comparison with initial diamond seeds. However, during air oxidation test (Thermoplus TG 8120) some features become discernible. The data of differential thermal analysis (DTA) are shown in Fig. 1. So, hydrogenation of initial diamond causes shift of oxidation reaction rate maximum (708 °C DTA effect) to higher temperature region in comparison with initial seeds. Increasing of oxidation resistance occurs due to removing of surface defects during hydrogenation at high temperature. The products after hydrothermal synthesis are characterized by small amount of amorphous carbon, which completely burned out until 600 °C, peak at 727 °C corresponding to 5000# h-diamond seeds. However, peak at 858 °C is important because it means that some coarse diamond grains appeared. Thus, DTA data are very effective for separation of different carbon materials. Moreover, during modeling tests we have found that DTA data are also sufficiently sensitive to the grain size of diamond subjected to air oxidation, and we have been able to make easily the apparent coarse diamond grains mixed with fine as base component.

The suggestion about coarsening initial seeds through hydrothermal reaction was confirmed after careful optic and electron microscopy studies of samples treated with two steps of acid processing. Fig. 2(c) demonstrates the scanning electron microscopy (SEM) images (HITACHI S-4700T) of diamond polycrystals shaped as globules and initial seeds (a, b) at approximately same magnification. It is obvious that globules were produced through sintering of initial 5000# seeds (Fig. 3(a)) and according to energy dispersive X-ray microanalysis (EDX) have no impurities besides carbon and oxygen similar to initial h-diamond seeds (Fig. 3(b)).

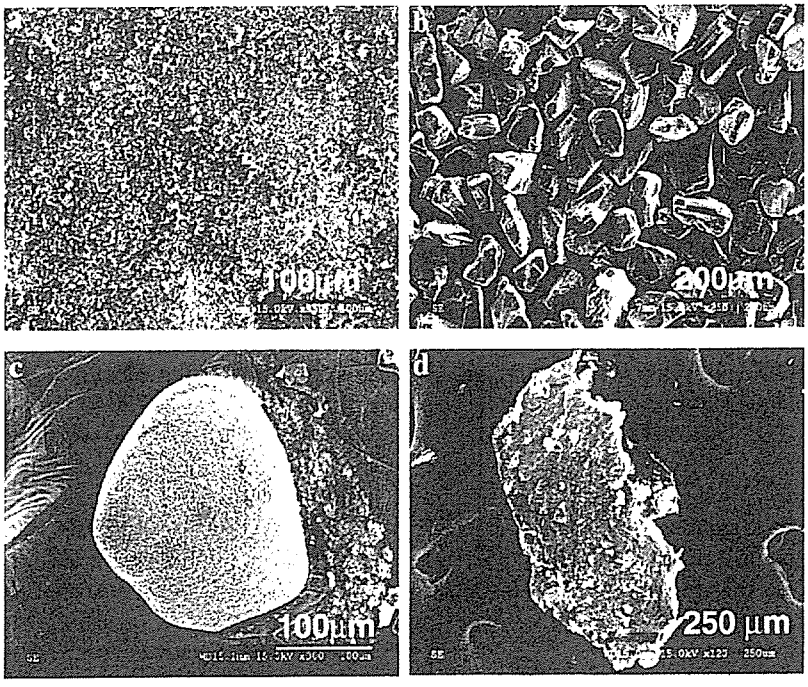

Fig. 2. SEM images showing size and shape of hydrothermal synthesis products after two steps acid treatment: c, d and initial seeds: a — 5000# and b — 325#.

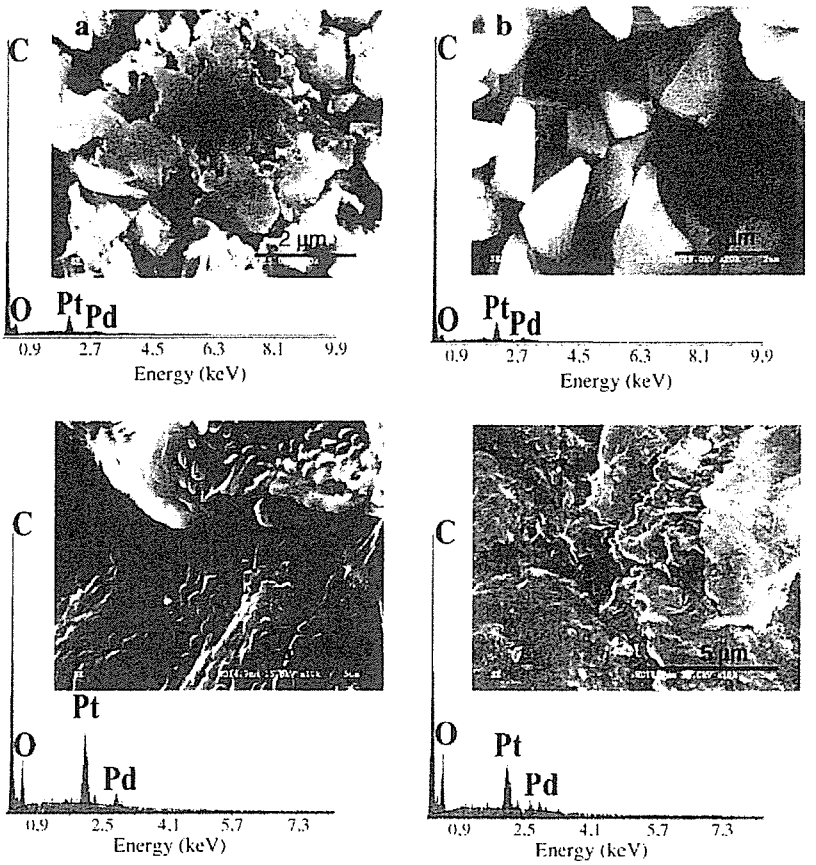

Fig. 3. Surface structure of hydrothermal products a, c, d and initial 5000# seeds b with appropriate EDX data; a — produced by sintering of independent seeds and c, d — grown on the surface of Cu-diamond pellets; a, c — after two steps acid treatment and d — after 24 h exposure in Aqua regia and heating up to 1000 °C in air.

More interesting results were obtained after experiments with fixed seeds. Brittle as ceramics transparent plates considerably differed in size, shape and surface morphology from used seeds have been elicited in acid treated reaction products (Fig. 2(d)). These carbon based 200–500 μm size plates (average size of 5000# and 325# seeds composes 1 and 45 μm, respectively) are certainly new growth, characterized by raised oxygen concentration in comparison with seeds and sintered globules (Fig. 3(c)). Furthermore, they have exhibited high stability similar to coarse 325# natural diamond seeds in air oxidation condition heating up to 1000 °C with heating rate 10°/min. Fig. 3(d) demonstrates the surface structure of large hydrothermal carbon plate after air oxidation with appropriate EDX data.

Sufficiently, large size of carbon plates has permitted us to separately expose to micro X-ray diffraction (μ-XRD) of everyone. So, according to μ-XRD data (JEOL JDX-3530, 30 μm collimator) and (M21X MAC Science Co., Ltd, 100 μm collimator) these plates have contained amorphous (Fig. 4) or perhaps nanocrystalline diamond phase, because the diamond growth outside its thermodynamic stability is preferably continued as nanocrystalline diamond-structured carbon with average size nanocrystals of 5–10 nm [5]. However, some plates were displayed (111) and (220) diamond peaks (Fig. 4(b, c)) even after heating up to 1000 °C in air (Fig. 4(b)). Of course, during growth the new phase can involve in some amount of seeds from the surface of copper templates. However, we did not find any presence of initial seeds on the surface of large plates, which were analyzed by μ-XRD. Moreover, the number of diamond grains in Cu-pellets surface layer was very few and cannot be estimated XRD. In addition, starting diamond powder 5000# completely disappeared after heating up to 1000 °C in air while hydrothermal produced diamond structured plates remained in unburned rest.

For full characterization of our process we have conducted the Raman analysis (at 532.07 nm laser wavelength) of reaction products grown on substrate other than diamond. In this case the 325# cubic BN was used as seeds. The Raman spectrum of two-step cleared

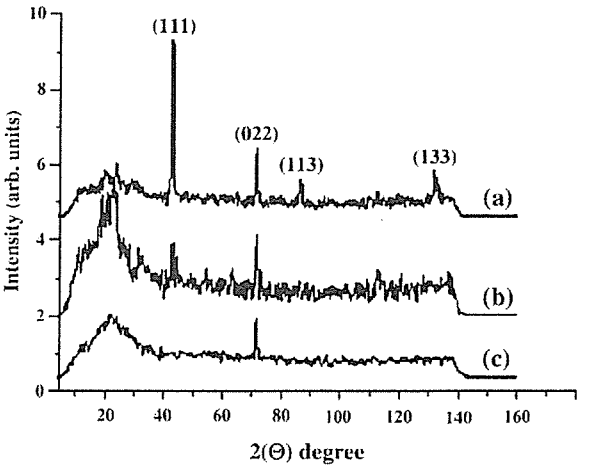

Fig. 4. Micro XRD patterns of hydrothermal carbon plates b, c and initial 5000# seeds a; b — after 24 h exposure in Aqua regia and air oxidation at 1000 °C; c — after two steps acid treatment.

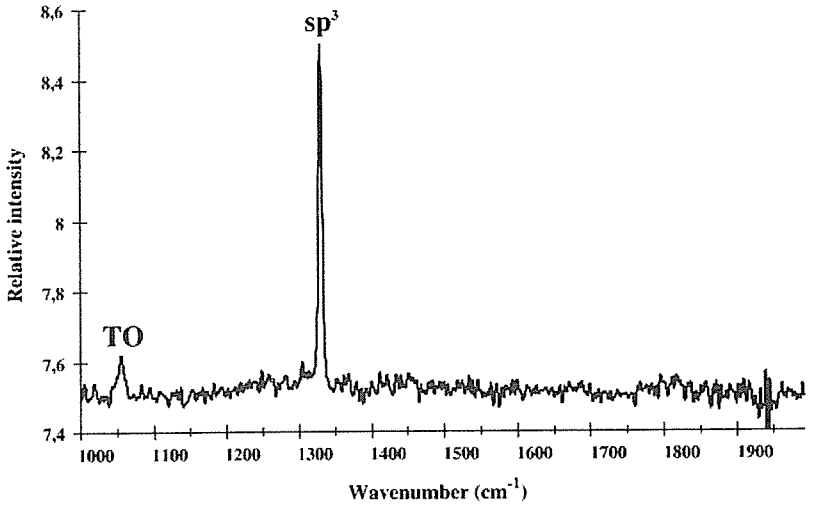

Fig. 5. Raman spectrum from diamond layer grown on cubic BN substrate during hydrothermal reaction at 1 GPa, 300 °C, 72 h. Sample was acid treated by two steps.

hydrothermal reaction products shown in Fig. 5 demonstrates a weak broadened TO peak from the BN substrate [16] and single narrow 1332 cm^{-1} peak that gives obvious evidence on the formation of diamond under hydrothermal conditions.

At this stage we do not know a mechanism for hydrothermal growth process. Perhaps, the mechanism of new diamond growth is condensation–polymerization. Firstly, 1,1,1-Trichloroethane easily decomposed under alkaline hydrothermal conditions [17], as a result the colloidal solution containing unstable and very active carbon can be produced according to the following equation:

$$C_2H_3Cl_3 + 3NaOH = 2C + 3NaCl + 3H_2O$$

Then diamond growth may occur by insertion of active C species into C–H bonds of hydrogen terminated diamond surface. For example, according to Ref. [18], the energy barriers for addition of C_2 to diamond surface are small during diamond thin film growth from fullerene precursors, and (110) hydrogen terminated diamond surface [18] or even bare substrate [18,19] is energetically very favorable for joining of carbon dimer. There is evidence that the growth proceeds mainly on the (110) face [20], and obviously this is a reason why hydrothermal products mostly revealed (220) reflection in μ-XRD pattern (Fig. 4(b, c)).

It should be noted that we did not use any catalyst metals (usual Ni–Fe–Mn or Co). Pure copper is not catalyst for diamond synthesis [21] and produced diamond is certainly free of metallic elements (according to EDX data) similar to natural diamond [12].

4. Conclusions

There are only few publications on the hydrothermal diamond synthesis. At present, only Szymanski et al. have produced the real low-pressure liquid phase epitaxy of diamond seeds. This study coordinates with the results of Szymanski's group and confirms that hydrothermal diamond growth is possible and should be involved in the origination of natural diamond.

As diamond-structured carbon has been synthesized using liquid organic precursor in soft hydrothermal conditions then the growth of diamond in Nature can be continued in colloidal pneumatolytic–hydrothermal environment [8].

Acknowledgements

The authors would like to thank Dr. G. Bignall for his assistance in preparing the manuscript.

References

[1] F.P. Bundy, H.T. Hall, H.M. Strong, Nature 176 (1955) 51.
[2] J.C. Angus, C.C. Hayman, Science 241 (1988) 913.
[3] G. Burkhard, K. Dan, Y. Tanabe, A.B. Sawaoka, K. Yamada, Jpn. J. Appl. Phys. 33 (1994) 1876.
[4] M.N. Regueiro, P. Monceau, J.-L. Hadeau, Nature 355 (1992) 237.
[5] Y.G. Gogotsi, S. Welz, D.A. Ersoy, M.J. McMallan, Nature 441 (2001) 283.
[6] Y.G. Gogotsi, P. Kofstad, M. Yoshimura, K.G. Nickel, Diamond Relat. Mater. 5 (1996) 151.
[7] R.C. DeVries, R. Roy, S. Somiya, S. Yamada, Transactions of the Materials Research Society of Japan 19B, Adv. Mater. 6 (1994) 641.
[8] A. Szymanski, E. Abgarowicz, A. Bacon, A. Niedbalska, R. Salacinski, J. Sentek, Diamond Relat. Mater. 4 (1995) 234.
[9] A. Szymanski, J. Chem. Vapor Depos. 4 (1996) 278.
[10] S. Korablov, K. Yokosawa, K. Tohji, N. Yamasaki, Trans. Mater. Res. Soc. Jpn. 29 (5) (2004) 2371.
[11] X.-Z. Zhao, R. Roy, K.A. Cherian, A. Badzian, Nature 385 (1997) 513.
[12] R.C. DeVries, Nature 385 (1997) 485.
[13] H. Sato, K. Uematsu, K. Watanabe, A. Saul, W. Wagner, J. Phys. Chem. 17 (1988) 1439.
[14] H. Kotsuki, H. Nishizawa, S. Kitagawa, M. Ochi, N. Yamasaki, K. Matsuoka, T. Tokoroyama, Bull. Chem. Soc. Jpn. 52 (1979) 544.
[15] T. Tsubota, O. Hirabayashi, S. Ida, S. Nagaoka, M. Nagata, Y. Matsumoto, K. Kusakabe, S. Morooka, Chem. Soc. Jpn. 11 (2001) 631.
[16] R.M. Erasmus, J.D. Comins, M.L. Fish, Diamond Relat. Mater. 9 (2000) 600.
[17] N. Yamasaki, T. Yasui, M. Matsuoka, Environ. Sci. Technol. 14 (1980) 550.
[18] P.C. Redfern, D.A. Horner, L.A. Curtiss, D.M. Gruen, J. Phys. Chem. 100 (1996) 11654.
[19] M. Sternberg, M. Kaukonen, R.M. Nieminen, Th. Frauenheim, Phys. Rev., B 63 (2001) 165414.
[20] C.J. Chu, R.H. Hauge, J.L. Margrave, M.P. D'Evelyn, Appl. Phys. Lett. 6112 (1992) 1393.
[21] K. Mallika, R.C. DeVries, R. Komanduri, Thin Solid Films 339 (1999) 19.

特集　材料のマイクロ/ナノ微細化と生体反応挙動

カーボンナノチューブの細胞内挙動

横山敦郎*

JJSB

Biological behavior of carbon nanotubes

The tissue response to multi wall carbon nanotubes (MWCNTs) and hat-stacked carbon nanofibers (H-CNFs) were investigated to evaluate biocompatibility of carbon nanosubstances. MWCNTs and H-CNFs were implanted in the subcutaneous tissue of rats. Histological and ultrastructural observations revealed that MWCNTs and H-CNFs were not acutely toxic in the subcutaneous tissue and englobed by phagocytes. Possibility of structural changes of H-CNF was shown, while those of MWCNTs was not. It was suggested that the size and structure of carbon nanosubstances influenced their biological behavior.

カーボンナノ物質に対する生体反応を明らかにするため，ハット積層型カーボンナノファイバー(H-CNFs)と多層カーボンナノチューブ(MWCNTs)をラット皮下組織に埋入し，組織学的，超微細構造学的に検索した．両者ともに，急性毒性は認められず，マクロファージにより貪食されることが示された．MWCNTsの構造には変化が認められなかったが，H-CNFsでは，短縮や構造の変化が生じている可能性が示され，ナノ物質のサイズや構造は，細胞内挙動に影響を与えることが示唆された．

*Atsuro Yokoyama**

Key words：多層カーボンナノチューブ(multi wall carbon nanotubes)，ハット積層型カーボンナノファイバー(hat-stacked carbon nanofibers)，生物学的挙動，超微細構造学的検索

1991年，Iijimaによって発見されたカーボンナノチューブ[1]は，その特徴的な電気的，物理的，および化学的性質から，工業界において注目を集め多くの基礎研究がなされている．生体材料としても，カーボンナノ物質の一種であるフラーレンやナノホーンは，DDSや遺伝子導入の際の担体として研究が進められている[2,3]．

筆者らも，カーボンナノ物質を生体材料として再生医療に応用すること，特に細胞培養用スカフォールドの開発を目的に研究を進めている[4~6]．生体材料にとって，安全性はいうまでもなく最も重要な所要性質であるが，ナノ物質の医学領域への応用に際して，ナノ物質の毒性やこれらの物質に対する生体の反応についての研究は少ないため不明な点が多く，ナノ物質に対する安全性はいまだ確立されているとはいいがたい．細胞毒性をはじめとする*in vitro*での報告がなされるようになり[7~9]，*in vivo*における生体反応も最近ようやく報告されるようになってきた[10~14](カーボンナノチューブに関しての毒性評価の詳細については，本号の田路・佐藤論文を参照されたい)．中皮腫などのアスベスト被曝長期後の病変が最近大きな社会問題になっていることからも，*in vivo*での研究は必須であると考えられる．このような状況から，筆者らは，再生医療への応用とともに，カーボンナノ物質に対する生体反応についての研究を行っている[15~19]．

本稿においては，皮下組織におけるカーボンナノ物質に対する反応，特に，カーボンナノ物質のサイズ(大きさ)と構造の違いによる細胞内挙動について述べたい．

筆者らが研究をはじめた当初は，カーボンナノチューブやフラーレンについて精製された状態での入手が困難であったこともあり，共同研究を行っている東北大学大学院環境科学研究科の田路研究室よ

* Department of Oral Functional Prosthodontics, Division of Oral Functional Science, Graduate School of Dental Medicine, Hokkaido University　北海道大学大学院歯学研究科口腔機能学講座口腔機能補綴学教室

[略歴]　1984年 北海道大学歯学部卒業．1988年 同 大学大学院歯学研究科修了(歯学博士)，同 大学歯学部助手．2002年 同 大学歯学部附属病院講師．2005年 同 大学大学院歯学研究科教授，現在に至る．専門：歯科補綴学，骨補填材，デンタルインプラントなどの生体材料に対する*in vivo*の反応，ナノ物質の生体材料への応用．趣味：読書